2020

An experimental study of debris-bed friction during glacier sliding

Anna Carrie Thompson
Iowa State University

An experimental study of debris-bed friction during glacier sliding

by

Anna C. Thompson

A thesis submitted to the graduate faculty

in partial fulfillment of the requirements for the degree of

MASTER OF SCIENCE

Major: Geology

Program of Study Committee:
Neal R. Iverson, Major Professor
Jacqueline E. Reber
Peter L. Moore

The student author, whose presentation of the scholarship herein was approved by the program of study committee, is solely responsible for the content of this thesis. The Graduate College will ensure this thesis is globally accessible and will not permit alterations after a degree is conferred.

Iowa State University

Ames, Iowa

2020

TABLE OF CONTENTS

Page

ACKNOWLEDGMENTS

First, I would first like to thank my advisor, Neal Iverson. His continued guidance and support on this research have made me a better scientist and writer. He, along with Luke Zoet, conceived of these experiments and secured funding from NSF. I was able to take many classes taught by Neal, which were all excellent. My committee members, Jacqueline Reber and Pete Moore, have also been excellent teachers and sources of support.

My lab mates, Charlotte Bate, Conner Adams, and Jacob Fowler, have contributed valuable ideas and assistance. Charlotte, in particular, was present for many ventures, predicaments, and breakthroughs. She has been a great friend and constant cheerleader from near and far. Similarly, Christian Helanow was a good mentor, friend, and ice-lifter. I also have to thank the many officemates who were willing to take small breaks from work to help lift large pieces of ice and teach me how to use a camera.

The content of this thesis was improved and expanded upon by conversations with Alan Rempel, Dougal Hansen, and Bernard Hallet. Thank you for your interest, patience, and time. Jacob Woodard and Wyman Martinek offered essential help when analyzing the microtopography of the rock bed. Additional thanks to the many people who have humored my unusual requests and occasional confusion when looking for and learning how to use new tools and equipment. The encouragement and resources offered by all of these people, and more, are responsible for the success of this thesis.

ABSTRACT

Modeling the speeds of sliding glaciers reveals major uncertainty to estimates of sea-level rise and landscape evolution. In sliding models, friction between ice-entrained debris and the bed is often overlooked. For the common case of sparse debris in basal ice, theories developed in the 1970s by G.S. Boulton and B. Hallet included contradictory treatments of the forces that push particles against the bed. Boulton assumed that these forces scale with effective pressure—the difference between ice pressure and water pressure in cavities beneath particles—whereas Hallet assumed these forces depend on the rate of ice convergence toward the bed from melting and bed-parallel stretching of ice on stoss surfaces. The resultant bed-normal drag on particles depends on movement of ice past them by regelation and enhanced creep of ice.

To test these contrasting hypotheses, a large ring-shear device was used to slide temperate ice with sparse debris over a smooth rock bed. Isolated gravel-sized till particles in contact with the bed were built into an ice ring (outer diameter = 0.9 m, width = 0.20 m, thickness = 0.24 m) that rotated at a steady speed. A fluid, with its temperature controlled to the nearest 0.01ºC, surrounded the ice chamber to keep the ice at its pressure-melting temperature. Meltwater drained to atmospheric pressure from the edges of the bed. During experiments, either the ice convergence rate or total bed-normal stress was incremented, and shear stress was measured until a steady value was attained. In separate rate-controlled tests without ice, the dynamic friction coefficient between the particles and the rock bed was measured.

Results indicate that friction between particles and the bed depends on convergence rate. In contrast, total normal stress has no effect on bed shear stress, in agreement with Hallet's model. However, water-filled cavities formed beneath particles rather than the regelation ice expected from Hallet's model. These observations can be explained by an adjusted model that

appeals to mass conservation in melt films that exist everywhere at ice-rock boundaries. While ice converges with the bed, melting at the tops of particles creates pressure gradients and flow within melt films that push particles against the bed. Higher convergence rates generate more melt that steepens pressure gradients. Film thicknesses are sufficient to neglect intermolecular interactions associated with premelting. Finally, by incorporating observed particle rotation, the adjusted model is made consistent with the experimental data and observations.

CHAPTER 1. INTRODUCTION

Global environmental indicators like sea-level change and carbon fluxes are driven largely by the continuous movement of glaciers over continents. Carbon fluxes are influenced by the erosion and comminution of rocks at glacier beds that accelerate weathering rates and tectonic uplift, and the delivery of ice to the ocean contributes to sea-level rise. In fact, glaciers and ice sheets are the dominant contributors to global mean sea-level rise (IPCC, 2019). Although there have been many efforts to model the contribution of glaciers to sea-level rise (Nick et al., 2013; DeConto and Pollard, 2016), the unpredictability of glacier movement is the largest uncertainty in modeling sea-level rise over the next century (Willis and Church, 2012). Models of past and future landscape evolution also depend strongly on mechanisms of glacier sliding (Egholm et al., 2009; MacGregor et al., 2009; Herman et al., 2011; Headley and Ehlers, 2015). Thus, improved models of both sea-level rise and landscape evolution will require a more refined understanding of glacier sliding.

Glaciers that slide on rigid bedrock are said to have "hard" beds, whereas those that slip on deformable sediments are said to have soft beds, and both kinds of glaciers cause environmental change. Hard-bedded glaciers, the subject of this thesis, can surge so that their sliding speeds increase by a factor of 10-100 (Kamb, 1987; Thøgersen et al., 2019), which accelerates landscape evolution and, in some cases, contributes to sea-level rise. Although many fast-moving ice streams are thought to be soft-bedded, Thwaites glacier, the Antarctic ice stream that contributes most to sea-level rise, was recently discovered to be partially hard-bedded (Muto et al., 2019). Higher basal drag was recorded on the hard-bedded portions of the bed than where the bed is soft (Koellner et al., 2019), so at Thwaites glacier and perhaps elsewhere in Antarctica

and Greenland, hard-bedded sliding may need to be considered explicitly in modeling future sea-level rise.

Glacier sliding

Hard-bedded glaciers typically move 3-400 m a^{-1} by sliding and deforming internally by creep (Weertman, 1957; Cuffey and Paterson, 2010). Temperate hard-bedded glaciers move primarily by sliding, so the goal of this research is to study the basal drag that controls that sliding speed. When glacier ice slides at its pressure-melting temperature, friction between clean ice and rock is classically assumed to be negligible, owing to the melt film (<100 μm thick) that lubricates the ice-rock interface (Weertman, 1957). Instead, basal drag is thought to be mainly a product of pressure gradients across bedrock bumps that drive ice deformation and regelation around them.

Friction between ice-entrained debris and the bed also contributes to basal drag (Hallet, 1981) (Fig. 1.1), however the magnitude of its contribution is poorly known. Debris is incorporated into basal ice by detaching from bedrock and becoming engulfed in the ice. Debris can also enter at the glacier margins through crevasses or be brought to the bed by basal melting (Shoemaker, 1986). Although debris is common at glacier beds (Fig. 1.2), subglacial debris-bed friction is neglected in classical sliding models, despite its potentially large influence (e.g., Weertman, 1957; Lliboutry, 1968; Nye, 1969, 1970; Kamb, 1970; Fowler, 1981; Gudmundsson, 1997). Debris-bed friction has been incorporated into some sliding models (Hallet, 1981; Shoemaker, 1986; Schweizer and Iken, 1992; Iverson et al., 2020) but generally without experimental constraints on the magnitude of friction. Herein, experimental results are presented that bear on debris-bed friction, particularly on the factors that control the magnitude of contact forces between particles and the bed.

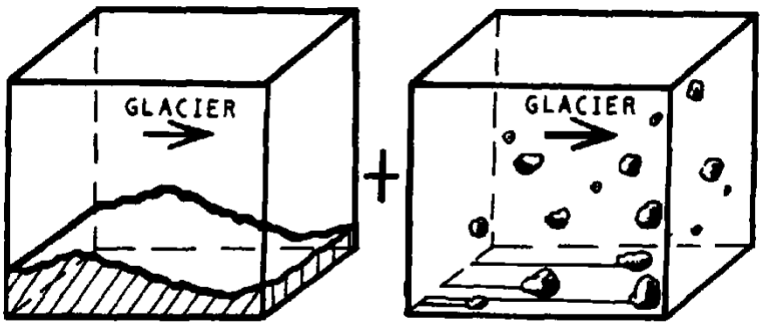

drag from bumps friction from debris

Figure 1.1. The two possible sources of glacier drag are undulations in bedrock topography and rocks scraping along the bed (illustration by Hallet, 1981). Glacial striations, pictured above from adjacent to Saskatchewan Glacier, Alberta, are always observed on sufficiently fresh glaciated bedrock and are evidence of rocks scraping against the bed. Photograph by Neal Iverson.

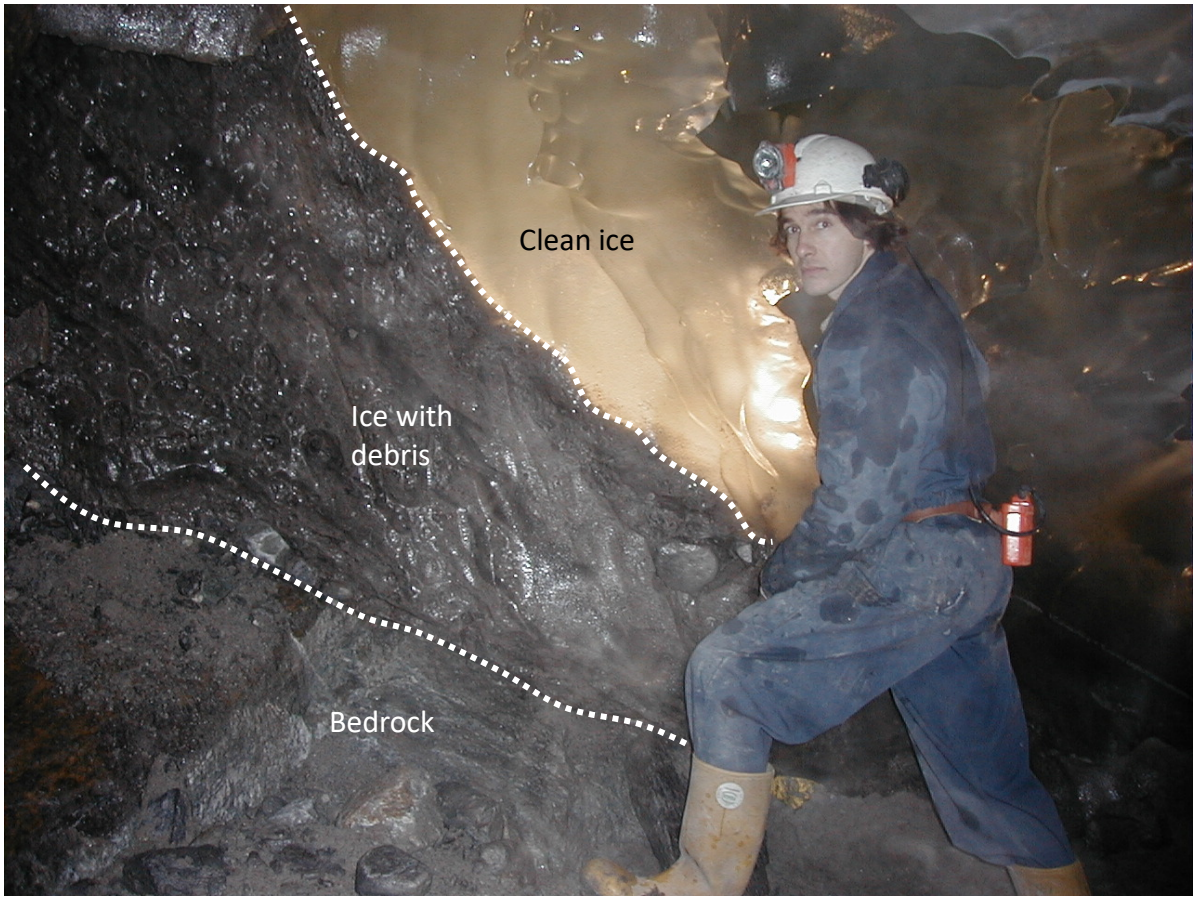

Figure 1.2. An example of ice containing basal debris in contact with the rock bed beneath the Svartisen ice cap in Norway. The debris concentration is about 10%. Photograph by Tom Hooyer.

Debris-bed friction theory

Before any direct data were available on the debris-bed contact forces that control debris-bed friction, two contrasting hypotheses were advanced by Boulton (1974) and Hallet (1979; 1981) that apply to isolated particles in contact with the bed. In either case, when ice contains debris, the following expression describes the local shear stress, τ_d, resulting from debris-bed friction:

$$\tau_d = \mu F_c c. \tag{1.1}$$

The shear stress depends on the friction coefficient between a rock particle and the bed, μ, contact force between a particle and the bed, F_c, and the areal concentration of particles at the ice-rock interface, c (number of particles per unit area). The two hypotheses differ as to what glaciological variable controls the particle-bed contact force: the local effective ice pressure on entrained particles (Boulton, 1974) or the convergence rate of ice toward the bed (Hallet, 1979, 1981).

Boulton (1974) proposed that the contact force depends on the effective pressure at the bed. The effective pressure is defined as the difference between the pressure exerted by ice on particles and the water pressure beneath particles at the bed surface. Neglecting the buoyant weight of particles in ice, he proposed a simple expression for particle-bed contact force:

$$F_c = (\rho_i g h - P_w)A. \tag{1.2}$$

The effective pressure is determined from the density of ice, ρ_i,, the gravitational acceleration, g, ice thickness, h, and water pressure at the bed, P_w. A is the area over which pressurized water can occupy cavities between particles and the bed. Under Boulton's model, particle speed along the bed can potentially be much lower than the sliding speed of the ice, if effective pressure is high and contact forces are, as a result, also high. For contact forces to be high in this model, water pressure in cavities between particles and the bed must be significantly lower than the ice pressure, $\rho_i g h$.

Boulton (1974) based his model on subglacial observations made by exploring passages on the lee sides of large bumps on glacier beds where ice separates from bedrock, allowing human access. There, he observed micro-cavities between particles and the bed that were fully drained, implying high effective pressure. Hallet (1981), however, argued that such observations were inherently biased because they were made down-glacier from bumps within passages at

atmospheric pressure and where the ice pressure on the bed was minimal, favoring micro-cavity development. In contrast, the stoss sides of bumps are where striations are deepest and most pervasive on deglaciated bedrock surfaces (Fig. 1.2) and where micro-cavities beneath particles, argued Hallet, would be less likely to form. If micro-cavities beneath particles do persist there, drainage of micro-cavities should be inhibited on stoss surfaces away from leeward zones of ice-bed separation, such that P_w is high and contact forces are low, as given by Equation 1.2. Deep, pervasive striations commonly observed on stoss surfaces, therefore, tend to contradict Boulton's (1974) model.

In contrast to Boulton's theory, Hallet (1979, 1981) considered particle-bed contact forces to be independent of effective normal stress and instead dependent on the convergence rate of ice with the bed. Convergence rate is the bed-normal component of ice velocity, which is a result of ice extending parallel to the bed as it deforms around bedrock bumps and of basal melting due to regelation, the geothermal heat flux, and frictional heating. G.K. Gilbert, in his study of crescent-shaped gouges on glacier beds, was the first to consider that the flow of ice around particles toward the bed imparted a viscous drag on them (Gilbert, 1906). This idea was embraced by Röthlisberger (1968) in his study of glacier erosion and is the basis of Hallet's models of subglacial friction and abrasion (Hallet, 1979, 1981).

In Hallet's model, contact force depends on regelation, enhanced ice creep, and the buoyant weight of particles in ice, which, even at low convergence rates, only contributes dominantly when particle diameters are as large as 0.2 m (Hallet, 1979). Ignoring the buoyant weight of particles, the contact force between particles and the bed is

$$F_c = \left(\frac{f 4\pi\eta R^3}{R_*^2 + R^2}\right) v_n \,, \tag{1.3}$$

so it is independent of normal stress and is linearly proportional to convergence rate, v_n. This proportionality is through the drag coefficient (in parentheses), which was derived by Watts (1974) and is predicated on an infinite body of ice deforming around an isolated particle by regelation and enhanced creep of ice, both of which are driven by deviatoric stresses induced in ice adjacent to the particle. The drag coefficient depends on the effective ice viscosity, η, particle radius, R, and the threshold particle size, R^*, at which drag per cross sectional area is greatest (~11cm) (Watts, 1974) owing to regelation and ice deformation past a particle being equally inefficient. The drag coefficient also includes a bed-influence factor, f, that adjusts the viscous drag to account for the particle sitting against a flat bed in an otherwise infinite ice body. One limiting factor of Hallet's model is that it requires particles to be isolated so that the flow fields of ice moving around them do not interact. This limits debris concentrations to less than ~15% by volume (Iverson et al., 2020).

In Hallet's model, the difference in the bed-parallel component of velocity between the ice and a rock particle is expected to be similar to the rate of ice convergence with the bed, making the rough and conservative assumption that the friction coefficient between a particle and the bed equals 1.0. Owing to convergence rates usually being a small fraction of the total sliding speed of ice, particles are expected to move at nearly the speed of the ice. Particles are expected to frictionally lodge on the bed (i.e., stop moving) only in the unlikely event that convergence rates with the bed are close to the sliding speed.

The buoyant weight of particles can often be neglected because it is not expected to be a substantial fraction of the contact force if particles are less than one meter in diameter (Hallet, 1979). If necessary, buoyant weight can simply be added to these models as a separate term in the equation for contact force (e.g., Hallet, 1979).

More importantly, by assuming particles are held rigidly in ice, Boulton (1974) and Hallet (1979; 1981) neglect particle rotation. Considering the extreme scenario of a smooth, spherical particle rolling in ice along the bed, like a ball bearing in a socket, particle rotation has the potential to reduce the shear stress that particles exert on the bed (see Equation 1.1) to zero. On the other hand, actual rock particles are, to some extent, angular and non-spherical. These are attributes that resist particle rotation. Nevertheless, the full friction possible beneath particles may not be attained, owing to particle rotation, and thus both models may over-predict shear stress between a glacier and its bed to some degree. Data to help constrain the extent of particle rotation in ice during glacier slip are not available.

Debris-bed friction field measurements

Field measurements of subglacial processes are limited by lack of access to the bases of glaciers. Installing instruments through boreholes is difficult because of uncertainties regarding the position of the bed and whether it has been disturbed. Measurements made at glacier margins, where the base of a glacier is sometimes more accessible, are not representative of conditions at the glacier bed as a whole.

In two cases, excavation of tunnels as part of hydropower installations has allowed access to the bases of glaciers away from their margins. Boulton et al. (1979) first attempted to monitor shear stress and normal pressure on a rock bed in the 1970s beneath Glacier d'Argentière, where the ice was 100 m thick. They installed transducers at the base of the ice and concluded that a measured proxy for shear stress could be connected to debris-bed friction (Boulton et al., 1979). However, because their sensors were not calibrated, the actual shear stress due to debris was not determined. In another study beneath Glacier d'Argentière, other authors observed that ice one or two meters above the ice-rock interface moved two or three times faster than where it was held back by friction at the bed (Vivian and Bocquet, 1973; Vivian, 1980).

Another access tunnel, excavated as part of a hydropower installation at the base of the Svartisen ice cap in northern Norway, allowed access to the base of the temperate outlet glacier, Engabreen, where it was 210 m thick (Iverson et al., 2003; Cohen et al., 2005). A debris-bed friction experiment was conducted by measuring sliding speed, water pressure, temperatures, and shear stress on a smooth granite tablet that was installed flush with the hard bed. The basal ice (Fig. 1.2) contained 11% debris by volume. Response of shear stress to changes in effective normal stress was recorded, implying that a bulk friction coefficient between the debris-laden glacier ice and the bed was 0.05. This value, however, was well below that required to account for the magnitude of the shear stress recorded (60-200 kPa). As such, particle-bed contact force was attributed to high rates of ice convergence with the bed that resulted from unnaturally high melt rates caused by warm tunnel air immediately beneath the instrument. The main limitation of these field experiments is that the actual condition of the ice-bed interface was poorly known because it could not be observed directly. For example, a thin (of order 1 cm) water-saturated till layer that separated the ice from the rock tablet could have developed with time, although such a till layer would have presumably resulted in a bulk friction coefficient equal to the till internal friction, > ~0.2 (Iverson, 2010), rather than a value as small as that measured (0.05).

Debris-bed friction experiments

The friction between clean ice and a smooth bed in relation to temperature below the pressure-melting temperature has been studied experimentally (McCarthy et al., 2017). At decreasing ice temperature below the pressure-melting temperature, friction increased linearly. Temperature measurements, however, had an error of ±1.8ºC (McCarthy et al., 2017), which is not precise enough to measure the friction at the pressure-melting temperature.

In other experiments the downward flow of ice around stationary spheres has been studied. Results support the hypothesis that convergence rate of ice with the bed influences

particle-bed contact force and therefore particle-bed friction (Iverson, 1990; Byers et al., 2012). Forces were measured as ice flowed downward around spheres that were about five cm in diameter and made of concrete and Delrin® (a plastic of low thermal conductivity to inhibit regelation). Both experiments indicated that the flow of ice imparted a drag on the spheres that depended linearly on ice velocity (Fig. 1.3).

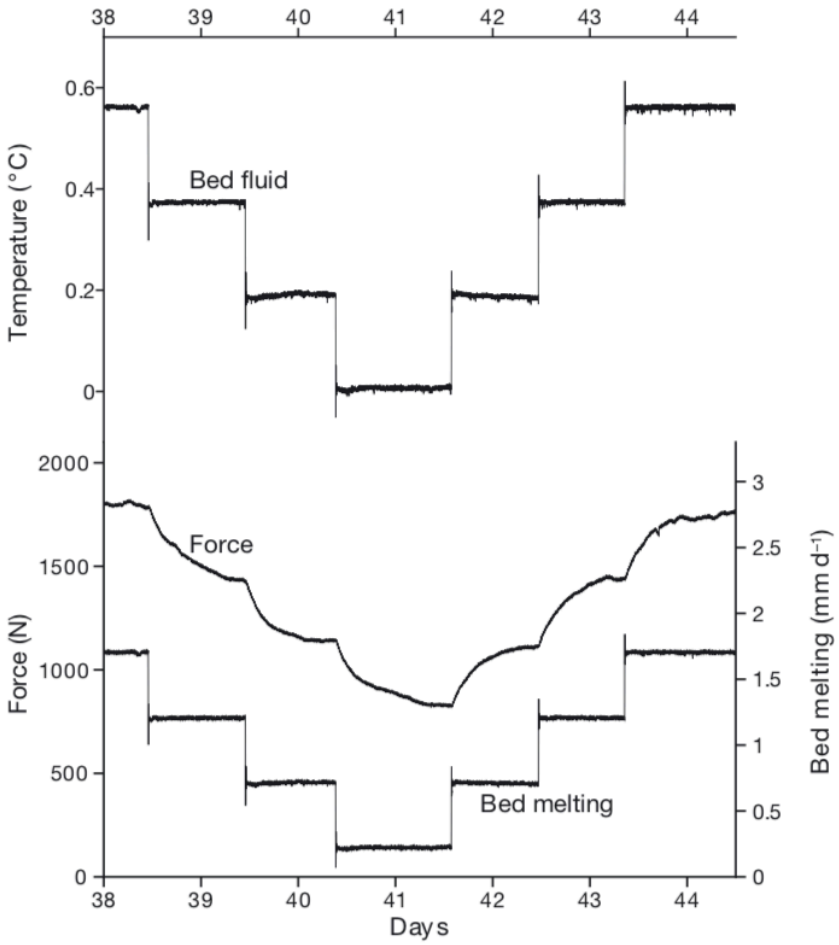

Figure 1.3. Stepped plots of melt rate and bed-sphere contact force from the Byers et al. (2012) experiments indicating that downward ice movement creates a downward drag on spheres (Byers et al., 2012).

In a complementary series of experiments, a block of ice at the pressure-melting temperature and containing isolated granite particles (angular, high sphericity, 30-40 mm

diameter) was slid at realistic speeds over a smooth marble bed (0.25 by 0.20 m) (Iverson, 1990). Convergence rate and normal stress were varied, and shear stress was recorded. Particles traveled 90-100% as far as the ice, and cavities formed beneath and on the lee sides of particles where regelation ice did not form. Many particles rotated, which sometimes accounted for up to 50% of their displacement. Overall, the results supported Hallet's theory that convergence rate controls debris-bed friction. However, only one particle size was used, and convergence rate never reached a steady state, so its relationship to contact force during steady flow was not measured.

Another experiment, in which a three-dimensional array of rock particles was frozen into sliding ice, confirmed that sliding ice can regelate downward past particles and influence particle-bed contact force (Iverson, 1993). In these experiments, gravel-sized particles were closely spaced so that ice movement around particles toward the bed was slower than the basal melt rate. This imbalance caused a continuous cavity to form at the bed.

Another series of experiments, which was designed to study the stick-slip behavior of ice containing debris on a rock bed, had different results (Zoet et al., 2013). Blocks of synthetic ice and blocks of glacier ice (sampled from the basal ice of a valley glacier) with up to 26% debris by volume were slid over a 4.5 by 5.0 cm polished granite surface in a series of direct-shear experiments. Meltwater was allowed to drain freely from the edges of the block, and the system was insulated to keep it within 0.5ºC of the target temperature. The experiments confirmed that meltwater lubricates the bed, but also indicated that particle-bed contact forces at the pressure-melting temperature depend on the bed-normal ice pressure. Again, however, the temperature control was not precise enough to confirm that the pressure-melting temperature was maintained, and it is possible that the system was at times too cold. Moreover, water at the bed, owing to its small area, drained over a distance of only ~2.5 cm to atmospheric pressure.

Experiments with rapidly sliding ice and smaller particles resulted in two regimes of bed shear stress that either did or did not depend on normal stress (Emerson and Rempel, 2007). River sediment was sorted into different size classes and frozen into ice discs (~11 cm diameter) at different concentrations to simulate basal ice. The discs were slid 0.3 m at 8.7 mm s^{-1} under different normal loads and at room temperature. Meltwater drained freely from the edges of the discs. Shear stress between the bed and ice containing particles less than 0.10 mm in diameter did not depend on normal stress. Particles of this small size were largely drowned by the melt film at the bed surface. If the concentration of any size particle (0.01-1.5 mm) was below 0.5% by weight, shear stress was also independent of normal stress. Shear stress depended on normal stress only if the ice contained larger particles, between 0.18 mm and 1.5 mm, and if their concentration was greater than 1% by weight. These experiments highlight the potential importance of debris concentration and the distribution of normal stress on the particles versus the melt-film thickness. Also worth noting is the very high sliding speed in these experiments and that the number of particles in contact with the bed increased over time as the ice melted. Moreover, owing to the lack of temperature control and low normal stresses, the melt film thickness, as scaled to particle size, was not realistic.

Hansen and Zoet (2020) studied debris-bed friction by subjecting blocks of sliding ice containing rock fragments to differing melt rates and normal stresses in a direct-shear device, like those commonly used in soil deformation experiments (Lambe and Whitman, 1979). In these experiments, a 10 by 10 cm limestone slab with five small drainage holes spanning its area was slid beneath ice containing 12 granite particles with high sphericity and angularity (diameter 9-11 mm) (Fig. 1.4). The device was housed in a cold room, and the rock was warmed from below to melt the ice. Where there was melting, the ice-rock interface was at the pressure-melting

temperature, but there was an upward temperature gradient, so some of the ice within 1 cm of the bed was below the pressure-melting temperature. The experiments indicated that shear stress depends strongly on melt rate, but there was also a significant relationship between shear stress and normal stress (Hansen and Zoet, 2020). The relationship between shear stress and melt rate was justified using theory appropriate for ice below the pressure-melting temperature adjacent to particles (Rempel and Meyer, 2019). The normal-stress dependence may have been due to angular clasts having greater contact area with the bed, bed roughness elements creating water pressure variations in the melt film and an uneven distribution of normal stress at the ice-rock interface, or drainage of water through holes in the bed that reduced water pressure in the melt film and in the cavities between particles and the bed (Hansen and Zoet, 2020).

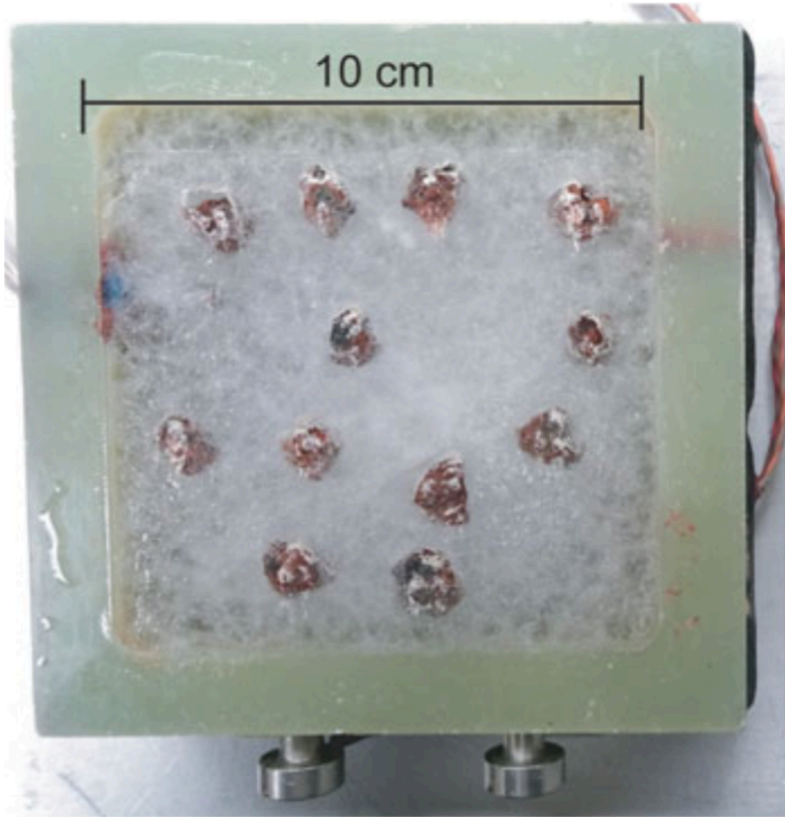

Figure 1.4. Ice-entrained particles in the Hansen and Zoet (2020) experiments. The ice block slid against a limestone tablet of the same size with five evenly spaced drainage holes (Hansen and Zoet, 2020).

Objective

The goal of this research is to improve glacier sliding theory by studying debris-bed friction experimentally, as a function of ice convergence rate with the bed and total normal stress for the case of a smooth rock bed. Although this case is unrealistic, it allows study of contact forces in isolation from bedrock bumps, which complicate interpretations by causing spatial gradients in both convergence rates of ice with the bed and local effective stresses. More importantly, bedrock bumps cause basal drag, so that the component from debris-bed friction cannot be easily isolated from the measured basal shear stress (Iverson et al., 2020).

With the experiments presented herein, we improve and expand on existing data by (1) maintaining all of the ice at its pressure-melting temperature at and away from the sliding interface, (2) maintaining the independent variable (convergence rate or normal stress) for 12-48 hours to ensure a steady-state relationship to contact force, (3) using a polished bed with asperities smaller than the melt film, (4) using till-derived particles that are sub-rounded, (5) sliding at realistic speeds, and (6) using till particles that are approximately the same hardness as the bed (the most common subglacial condition). Furthermore, these experiments are distinguished by their drainage conditions: meltwater is allowed to drain freely from the edges of the bed but over distances that are long relative to past experiments and that are closer to those that likely apply subglacially.

Hypothesis

The primary hypothesis tested herein is derived from the leading model of debris-bed friction (Hallet, 1979, 1981): that contact forces depend on convergence rates of ice with the bed and are independent of the effective pressure at the bed. Ancillary hypotheses of this model are also tested, namely that the particle-bed friction coefficient sets the magnitude of debris-bed friction and that particles move along the bed at a speed close to that of the sliding ice.

CHAPTER 2. METHODS

In these experiments, subglacial slip at the interface between a smooth rock bed and ice at its pressure-melting temperature is simulated. A ring-shear device with sensitive temperature control and unlimited slip displacement is used to rotate a large ring of ice across the bed under an applied normal stress. Till particles are frozen into the ice in contact with the bed to study how particle-bed contact forces respond to changes in basal melt rate and normal stress on the ice. Temperature, sliding speed, basal melt rate, normal stress, and bed shear stress are measured continuously, and particle-bed contact forces are inferred from the shear stress supported at the bed surface during slip.

Apparatus

The ring-shear device, which is housed in a cold room, accommodates a large ring of ice prepared in situ in an aluminum walled chamber that is 0.25 m deep, with a 0.9 m outer diameter and 0.5 m inner diameter (Fig. 2.1) (Iverson and Petersen, 2011). The inside surfaces of the ice chamber walls are polished smooth, while the outside surfaces are insulated by polyethylene closed-cell foam. A polished garnet-gneiss slab is fixed to the base of the chamber and is the smooth hard bed over which ice slides. Every 15 minutes for 10 seconds, cameras behind quartz glass windows allow direct observation of ice movement by capturing images of beads frozen into the outer edges of the ice ring (the short period is limited by the camera lighting as a source of heat, which would otherwise melt the ice undesirably fast). Water is allowed to drain freely from the edges of the bed to a reservoir at atmospheric pressure through ports beneath the rock bed and through 12 uniformly spaced ports in the chamber walls at the approximate elevation of the bed surface.

The ice chamber sits within a rigid loading frame consisting of two vertical columns, each 2.9 m tall, that support both the shear and normal stresses within the chamber (Fig. 2.1). A hydraulic press is mounted on two beams of heavy steel channel that connect the bases of the pillars. Two motors, a drive shaft, and an upper platen are suspended above the ice chamber by a yoke that spans the vertical pillars. The yoke can be raised and lowered up and down the pillars by a motor-driven winch and cables. It can be fixed in place with removable rods at multiple heights so the platen can be set low during experiments or set high to allow access to the chamber.

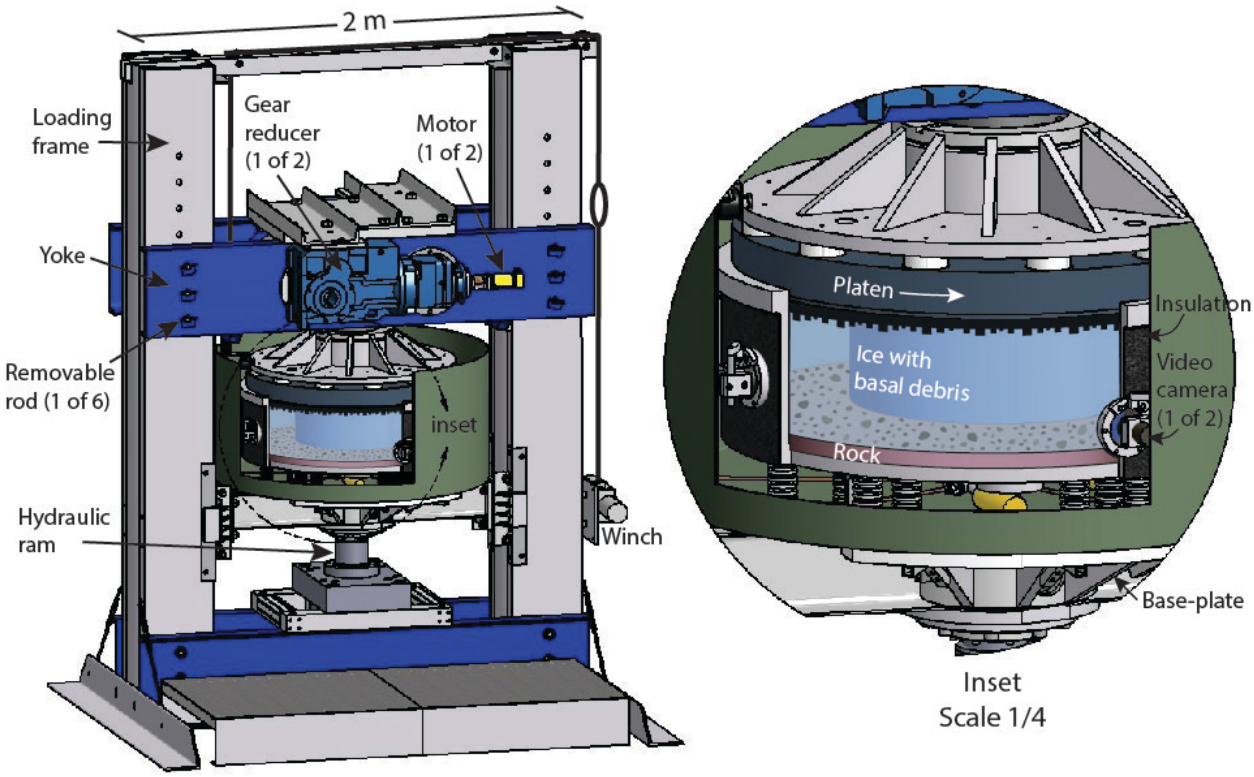

Figure 2.1. Ring-shear device with a cutaway view of the ice chamber. Wiring, plumbing, the controller for the hydraulic ram, and heating/cooling circulator for the glycol/water mixture, are not pictured. Debris is depicted at the sliding interface where the ice is in contact with the rock bed.

During experiments, the ice ring is rotated at a constant speed by the upper platen that has teeth to grip the ice. The platen rotation is driven by a central shaft that is turned by two geared-down electric motors. The platen is made of a strong high-density plastic called Delrin® with a low thermal conductivity that protects the ice ring from temperature fluctuations in the cold room and inhibits slip by regelation past the teeth of the platen. Slip instead occurs at the smooth rock bed and ice chamber walls. Normal stress is applied vertically to the ice ring by the 200-ton hydraulic press that pushes up on a base plate that supports the ice chamber and surrounding tub (green in Fig. 2.1).

The temperature of the ice ring and heat flow through it are precisely controlled to keep it at its pressure-melting temperature without melting the ice too quickly. During experiments, the cold room cycles between 0 and 2°C. To protect the ice ring from these large fluctuations, the sides and base of the ice chamber reside in a tub containing a circulating water/ethylene-glycol mixture. The ice chamber is supported by steel legs to allow the fluid to flow around and underneath it. The temperature of the water/ethylene-glycol fluid is regulated outside the cold room by an 18 L heating/cooling circulator (Lauda Proline model RP1840) with a precision of 0.01°C. The circulator pumps the fluid beneath the ice chamber to a distributing manifold at the base of the tub, and the fluid is returned through overflow valves near the top of the ice chamber. The temperature of the fluid in the tub is recorded by a high precision thermistor (0.0001ºC), although the foam insulation on the outer walls of the ice chamber keeps the ice-chamber walls even more uniform in temperature than the circulating fluid. Temperature variations in the fluid are of order 0.01-0.1ºC.

Ice temperature is measured with glass bead thermistors (Measurement Specialties model #55004) mounted flush with the chamber walls where they contact the ice. Thermistors are

spaced so that temperature is monitored in at least two locations on the inner and outer walls. The thermistors are arranged in a full-bridge circuit and calibrated in an ice-water bath with the high-precision thermistor. After their calibration, the accuracy of the thermistors is ~0.01ºC, although they can drift and sometimes become unstable with time.

Normal stress is measured with a load cell connected to the top of the piston on the hydraulic press that pushes upward on the ice chamber. During slip, shear stress is measured with a sensor that records the torque required to turn the upper platen. Rotation of the platen is measured manually from millimeter graduations on its outer edge. A vertical bead string frozen in the ice records any shear deformation of the ice that might occur during slip of ice over the bed. Finally, the vertical position of the ice chamber, which changes as the volume of the chamber contracts as meltwater drains from the bed, is measured continuously with a linear variable displacement transformer (LVDT) (RDP Group model LDC1000A).

Experimental procedure

To build the ice ring, deionized water is frozen in successive 1.5-2.0 cm layers in the ice chamber. Before freezing, the water is seeded with snow to encourage growth of randomly oriented crystals. Beads are frozen into each layer where they will be visible to the cameras and thereby allow tracking of ice motion about 10 cm above the bed surface. After 8-9 ice layers have been added, a final water layer is added, the upper platen is lowered into position by the yoke, and the ice chamber is raised by the hydraulic cylinder until the upper platen is in place within the ice chamber. The water freezes around the teeth of the upper platen under an applied normal stress, coupling the platen to the ice ring. Over the following six days, the ice ring is brought up to its pressure-melting temperature by setting the cold room to 1.0ºC and setting the external circulator so that it delivers fluid to the tub at a temperature of ~0.01ºC. The wall thermistors confirm that the pressure-melting temperature of the ice has been reached by

recording temperature decreases in response to applied increases in normal stress on the ice. Once the pressure-melting temperature is reached, the upper platen, along with the ice ring, are rotated at a steady speed of 7.6 m a^{-1} (referenced to the radial centerline of the ice ring). Experiments last 2-3 weeks, during which ice is displaced up to 50 cm (23% of a full rotation).

During experiments, ice converges with the bed due to basal melting and melting along the chamber walls. As noted in the introduction, the associated convergence rate is thought to be a primary independent variable controlling particle-bed contact forces (Hallet, 1979, 1981). During some experiments or parts of experiments, the ice is subjected to a range of realistic convergence rates, controlled by adjusting the temperature of the circulating bath. In other parts of experiments, the normal stress on the ice, suggested by other researchers to control particle-bed contact forces (Boulton, 1974; Zoet et al., 2013), is adjusted with the hydraulic cylinder. Generally, an adjustment in convergence rate or normal stress is made every 12 to 48 hours. Adjustments are usually followed by an initial peak in shear stress (Figs. 2.2 and 2.3), and then by shear-stress variability that settles around a long-term value without a clear trend. This long-term "steady" value is calculated from the average shear stress following its peak and before the next adjustment in convergence rate or normal stress. The standard deviation of the measured shear stress is calculated during these intervals to provide error bars.

The LVDT and video cameras are used to measure contraction of the sample chamber and convergence of ice toward the bed, respectively. The LVDT continuously measures the vertical position of the ice chamber, which rises as the ice ring contracts, and reflects melting on the top, base, and sides of the ice ring and meltwater drainage. For a given period of steady contraction and shear stress, a representative contraction rate and standard deviation are determined by fitting a regression line to the LVDT position data extending a day and a half

around the midpoint of that period. The video cameras in the chamber walls, which track the downward movement of beads in the ice, record the convergence rate, due exclusively to melting at the base of the ring and along the walls below where beads are observed. Convergence rate is calculated for each bead in the ice from its vertical position as it enters and exits the frame.

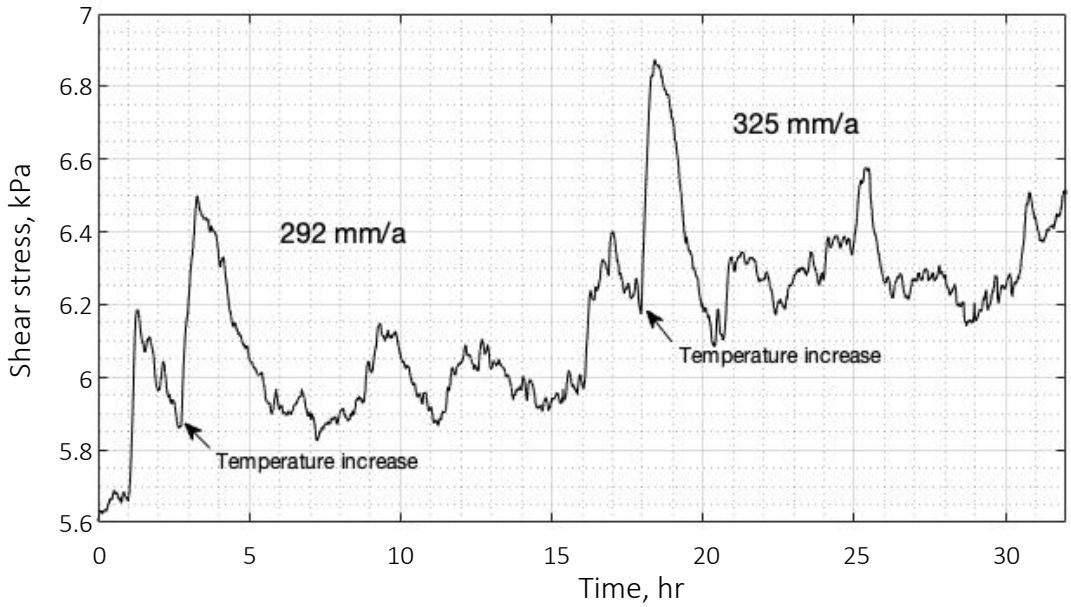

Figure 2.2. An example time series of shear stress after two increments of convergence rate. The temperature of the water/glycol bath was increased at the indicated times, which were followed by peaks in shear stress.

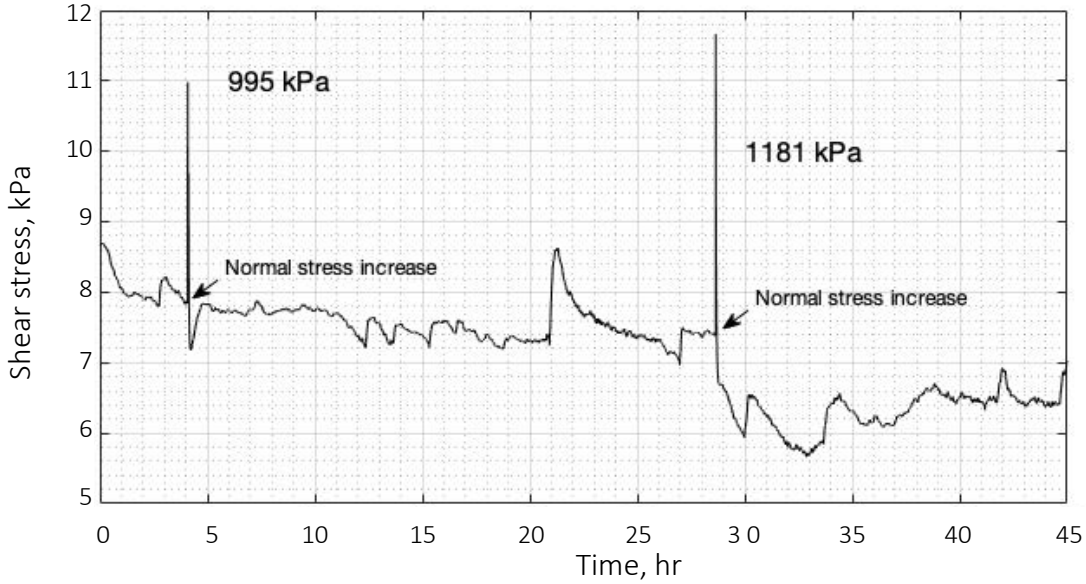

Figure 2.3. An example time series of shear stress during two increments in normal stress on the ice ring. Shear stress briefly peaks immediately after normal stress increases.

Contraction rates are measured continuously with the LVDT, but convergence rates—the variable of interest thought to control particle-bed contact forces—can be measured only sporadically with the video cameras and with a great deal more effort. Therefore, the sporadic convergence-rate record is used to calibrate the continuous contraction rate-record, so convergence rate can be inferred from contraction rate (Fig. 2.4) (recalling that convergence rate reflects melting at the base of the ice and along the lower portion of the walls, while contraction rate reflects melting on all surfaces of the ice ring). Multiple beads pass through the frame of the video camera during the periods used to measure contraction rate, so a representative convergence rate and standard deviation are calculated using an average, weighted for the amount of time each bead spends in view during the period being analyzed. Contraction rates and convergence rates are linearly related (Fig. 2.4). The standard deviations of each variable are propagated through the calibration.

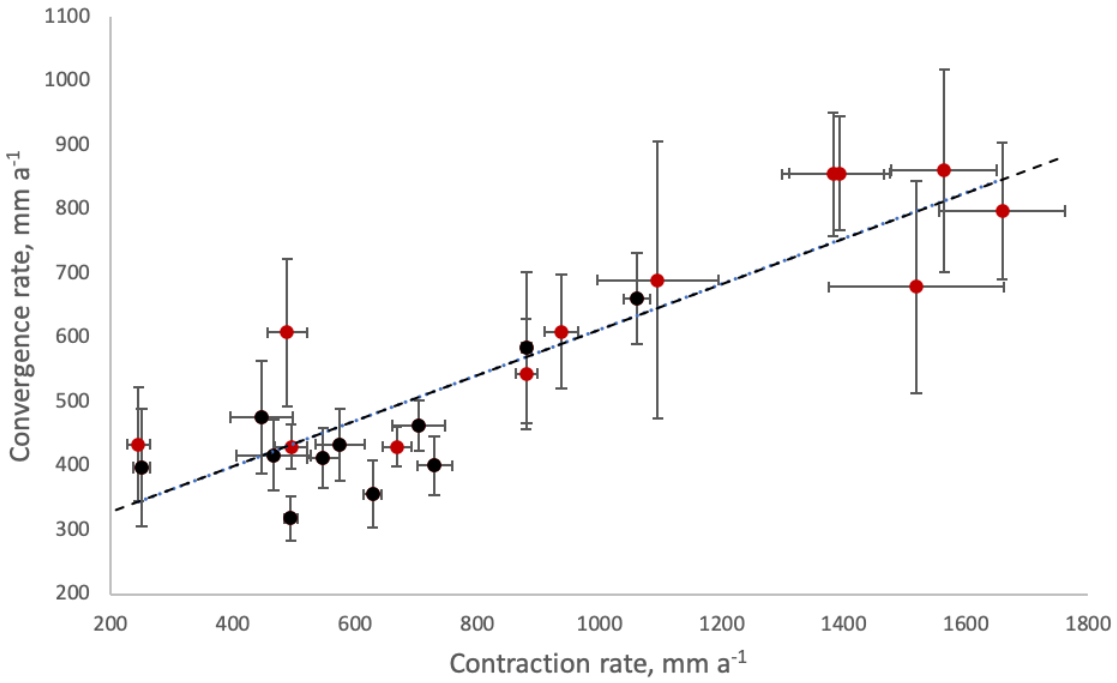

Figure 2.4. The relationship between convergence rate and contraction rate. Data are compiled from two experiments, indicated in black (Experiment 1) and red (Experiment 3). The coefficient of determination (R^2) and standard error are 0.78 and 82 mm a^{-1}, respectively. Error bars are one standard deviation.

Incorporating debris

Before incorporating rock particles in the ice, experiments were run with debris-free ice to measure the drag associated with the chamber walls and base under a range of normal stresses. Although the surface roughnesses of the chamber walls and rock bed are small, long-term use has subjected them to scratches and dents that introduce some drag that is part of the shear-stress measurement. The shear stress measured in experiments with a clean ice ring for a given normal stress is subtracted from the total shear stress measured during experiments incorporating debris. The remaining shear stress is then the friction only from debris added to the ice.

In experiments with debris, particles from Superior lobe till (Lusardi and Dengler, 2017) sit in contact with the smooth rock bed at the base of the ice. These particles are sub-rounded (Powers, 1953), a characteristic of many tills. Carbonate particles are removed so the hardness of the remaining metamorphic and igneous clasts is more comparable to the gneissic slab. The rock particles are sorted into small (8±3 mm minimum diameter), medium (16±4 mm minimum diameter), and large (24±4 mm minimum diameter) size categories. In experiments, the size distribution of the particles follows that observed by Hooke and Iverson (1995) in till samples, using a fractal dimension of -2.9. Particles are spaced at least 1.5 times their diameter apart from one another so that the flow fields within the ice moving around them are isolated (Fig. 2.5). Medium and large particles are numbered to track displacement. In Experiment 4, lines drawn on large particles trace their circumferences parallel to the bed, marking their original orientations to identify whether or not they rotate by the end of the experiment. Once positioned in contact with the rock at the base of the chamber, particles are frozen in place by the first layer of ice. The rest of the ice ring is constructed with clean ice so the number of particles in contact with the bed does not change over time.

Because the particles are frozen in a two-dimensional plane in contact with the rock, the volumetric concentration has to be approximated. Each particle is allocated a proportional area of the rock bed, weighted by its diameter. The radius of a circle with that area is used as a representative height to calculate a simulated ice volume associated with each particle and its allocated area of the rock bed. The volumetric concentration of debris is calculated from the total volume of debris and total simulated ice volume. By this method, the approximated volumetric concentration of debris is 3.6%.

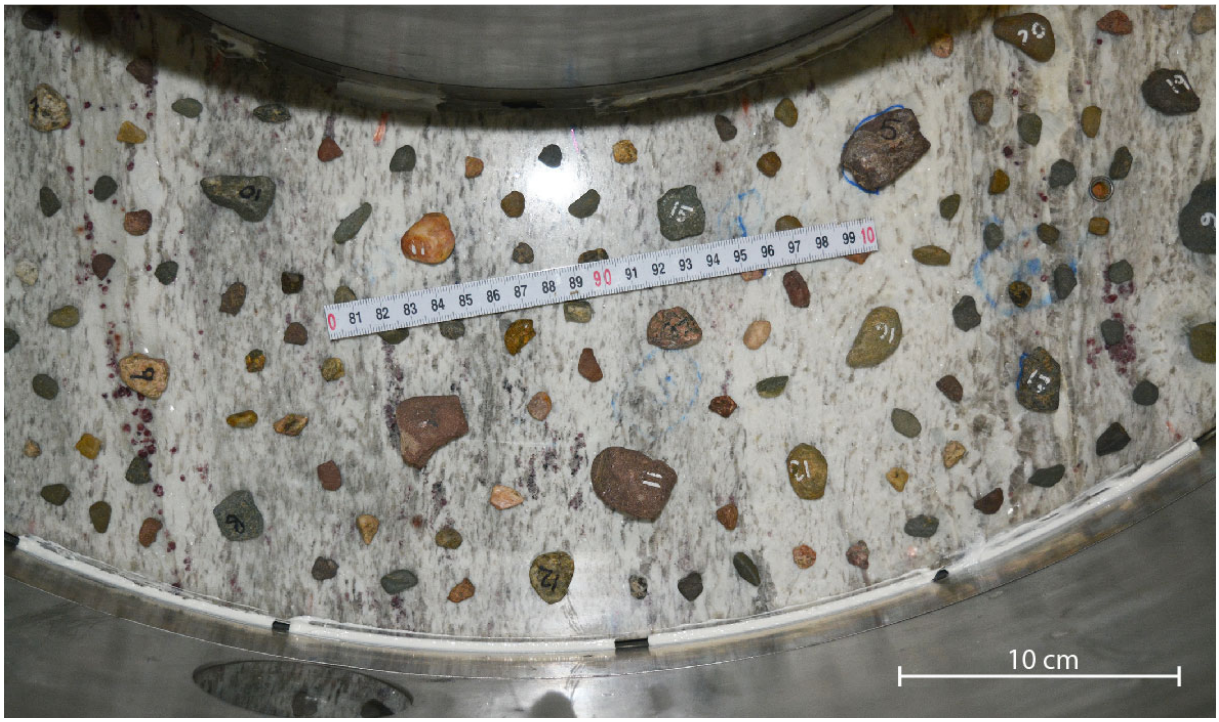

Figure 2.5. Till-particle placement on the base of the ice chamber before building the ice ring, looking downward into the ice chamber. The width of the chamber is 20 cm from wall to wall.

The dynamic friction coefficient between the particles and the rock bed is required to relate measured shear stresses to particle-bed contact forces. This friction coefficient is measured in separate rate-controlled experiments in which rock particles alone are slid over the rock bed. Thirty-four till particles are epoxied into a rigid slab that allows them to rest in contact

with the flat bed while not rotating during slip. The slab is slid at a constant speed of 13 m a^{-1} over the rock bed using a ball screw and geared-down motor. A normal force is applied to the slab while a load cell records the force required to push the slab across the bed. The friction coefficient (ratio of shear to normal force) is determined by conducting experiments over a range force comparable to contact forces measured in the ring-shear experiments. A fit to the data yields a friction coefficient of 0.37 (Fig. 2.6).

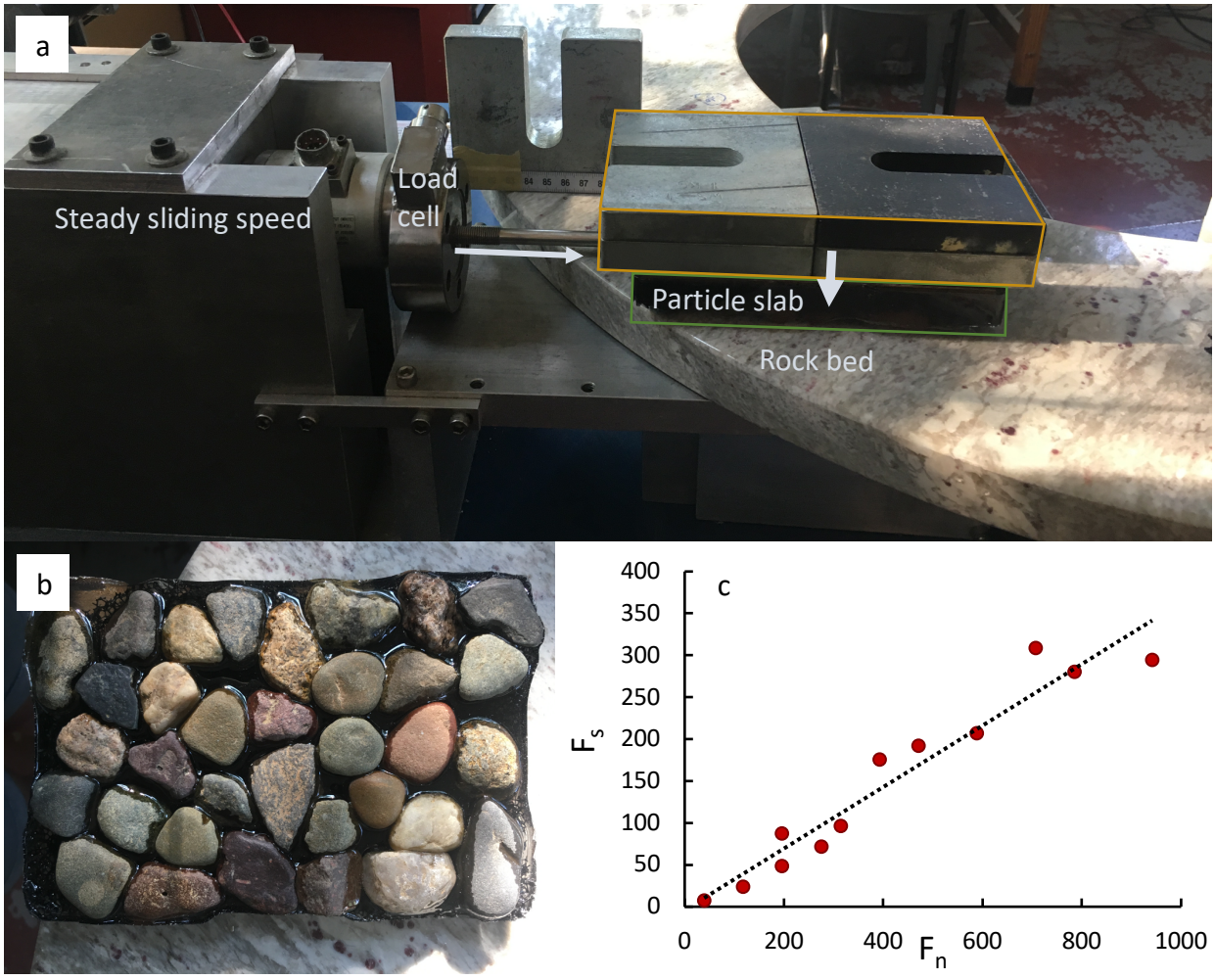

Figure 2.6. (a) Experimental set-up for measuring the friction between rock particles and the rock bed. A ball screw, with a load cell at its head, pushes the particle slab, loaded with weights, across the rock bed. (b) The bottom of the inverted particle slab. (c) Results, with a regression that implies a dynamic friction coefficient of 0.37.

CHAPTER 3. RESULTS

Control experiments with clean ice

Two control experiments were run with no debris in the ice, and four experiments were conducted with debris frozen into the ice in contact with the bed. In experiments with clean ice, shear stress was measured as normal stress was stepped up or down. The associated friction coefficient was used to estimate the component of shear stress from the experiments with debris that was not due to debris-bed friction. The first experiment with clean ice was followed by three experiments with debris, during which the ice chamber suffered a few scratches, and the rock bed became mildly striated and developed a crack. To measure the drag from these additional imperfections, a second clean-ice experiment was conducted before the final experiment with debris in the ice.

In both clean-ice experiments, shear stress increased only slightly with normal stress, such that the friction coefficients were 0.0045 and 0.0087 in the first and second experiments, respectively (Fig. 3.1). These values are about two-orders of magnitude smaller than those measured in friction experiments with rocks at room temperature (Jaeger et al., 2007).

Experiments with debris

In three experiments with debris at the base of the ice ring, convergence rates of ice with the bed were varied by changing the temperature of the circulating bath. Normal stress was 950-980 kPa and did not fluctuate more than 5 kPa during any single experiment. In the first experiment, convergence rate was increased incrementally. Convergence rates in the third and fourth experiments spanned a greater range. Overall the experimental range of convergence rates was 350-1220 mm a^{-1}. These values are of the same order as those expected on the stoss surfaces of bedrock bumps, where enhanced basal melting and ice thinning parallel to the bed cause ice

convergence rates with the bed that are significant fraction of the sliding speed (Iverson et al., 2020). After each adjustment of convergence rate, shear stress was allowed to stabilize for at least seven hours before making the next adjustment. The full time series of shear stress, normal stress, and vertical position can be found in the appendix, and measurements made during each period of stability are summarized in Table 3.1.

In all experiments, there was a clear positive relationship between convergence rate and shear stress (Fig. 3.2). A linear fit to the data has the form $\tau_d = 0.007\ v_n + 3.61$ with a coefficient of determination (R^2) of 0.87, indicating that convergence rate (v_n) accounts for 87% of the variation in shear-stress due to debris-bed friction. Notably, the fitted relationship does not pass through the origin, such that shear stress is 3.6 kPa at zero convergence rate. This non-zero y-intercept requires an explanation.

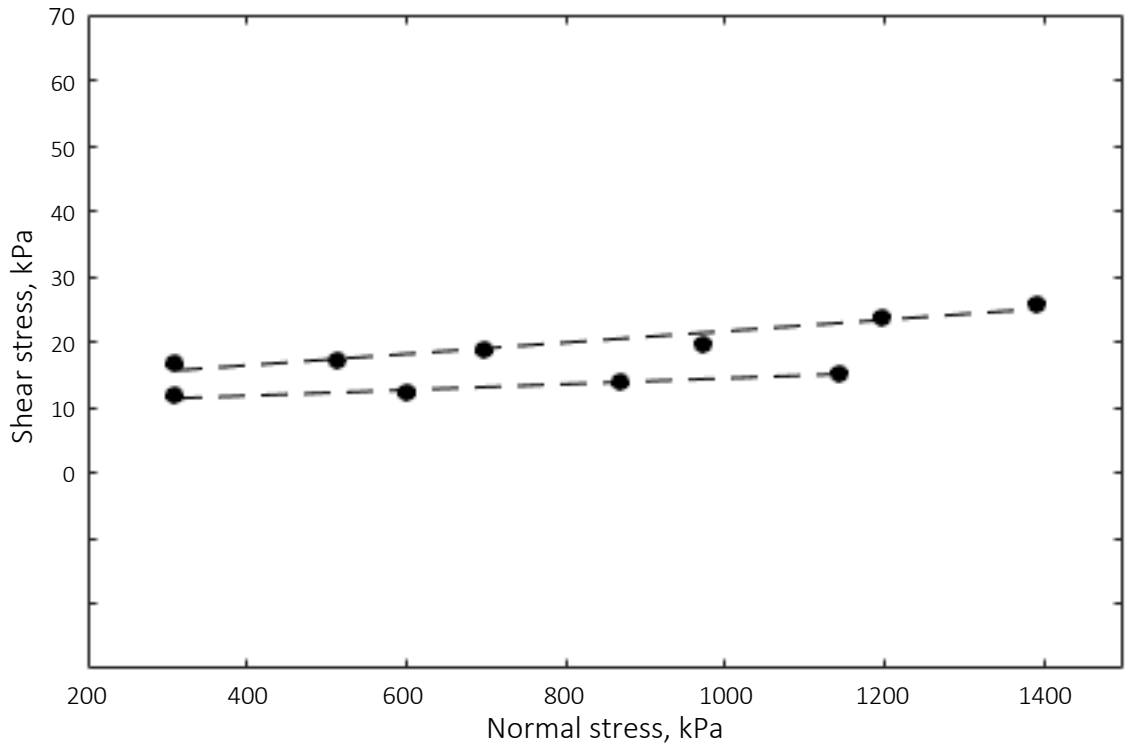

Figure 3.1. Shear stress as a function of normal stress in the two clean ice experiments. The fitted relationships were $\tau_d = 0.0045\ \sigma_n + 9.96$ and $\tau_d = 0.0087\ \sigma_n + 12.9$, respectively.

Table 3.1. Summary of measurements made during periods of stability between adjustments. Experiment 1 included a sequence of convergence rate adjustments followed by a series of normal stress adjustments. Experiment 2 included only normal stress adjustments. Experiments 3 and 4 included only convergence rate adjustments.

Experiment 1 Summary					
Stable period	**Shear stress (kPa)**	**Normal stress (kPa)**	**Convergence rate (mm a^{-1})**	**Duration (days)**	**Notes**
1	5.85	981	444	0.6	‣ Begin sequence of convergence rate adjustments.
2	5.91	980	425	0.4	
3	6.44	980	482	0.6	
4	6.95	979	500	1.0	
5	8.79	980	568	1.0	
6	9.31	980	637	0.9	‣ End sequence.
9	8.37	1259	456	1.2	‣ Begin sequence of normal stress adjustments.
10	7.54	613	348	1.7	
11	7.78	768	386	0.9	
12	7.97	995	468	1.0	
13	6.99	1181	432	0.9	‣ End sequence.

Experiment 2 Summary					
Stable period	**Shear stress (kPa)**	**Normal stress (kPa)**	**Convergence rate (mm a^{-1})**	**Duration (days)**	**Notes**
1	5.43	978	621	0.9	‣ Begin sequence of normal stress adjustments.
2	5.22	546	399	0.9	
3	4.94	697	583	0.3	
4	5.40	875	581	1.0	
5	7.87	1015	790	0.3	
6	8.24	1198	868	0.6	
7	8.41	1296	821	0.3	‣ End sequence.

Table 3.1 continued

Experiment 3 Summary					
Stable period	**Shear stress (kPa)**	**Normal stress (kPa)**	**Convergence rate (mm a^{-1})**	**Duration (days)**	**Notes**
1	6.88	961	438	1.3	‣ Begin sequence of convergence rate adjustments.
2	7.13	962	464	0.7	
3	7.55	963	505	1.0	
4	7.72	960	564	2.1	
5	7.97	959	618	0.9	
6	9.91	959	898	0.8	
7	6.77	958	352	3.7	
8	10.49	957	792	0.3	
9	7.78	958	535	0.3	
10	10.93	955	1059	0.3	
11	7.40	956	662	0.4	
12	12.20	954	1218	0.3	‣ End sequence.

Experiment 4 Summary					
Stable period	**Shear stress (kPa)**	**Normal stress (kPa)**	**Convergence rate (mm a^{-1})**	**Duration (days)**	**Notes**
5	5.43	967	448	1.9	‣ Begin sequence of convergence rate adjustments.
6	6.01	967	398	1.3	
7	7.68	967	553	0.8	
8	8.06	967	651	1.2	
9	8.46	966	780	2.1	
10	9.87	965	892	0.7	
11	10.65	965	1012	1.0	
12	10.54	963	1105	1.0	‣ End sequence.

In experiments with debris in ice, only small variations in shear stress occurred in response to normal stress changes, and measured shear-stress changes were not consistent with the direction of change in normal stress or the magnitude of the change. A second experiment confirmed the weak relationship between shear stress and normal stress over a larger range (Fig.

3.3a). The first experiment indicated a bulk friction coefficient that was only 0.0003 between the rock bed and the ice ring containing basal debris. The second experiment indicated a bulk friction coefficient that was larger but still small, 0.0049. Recalling that the friction coefficient for the first experiment with a clean ice ring was 0.0045, the addition of debris to the ice ring evidently had almost no influence on the friction between the ice ring and the bed.

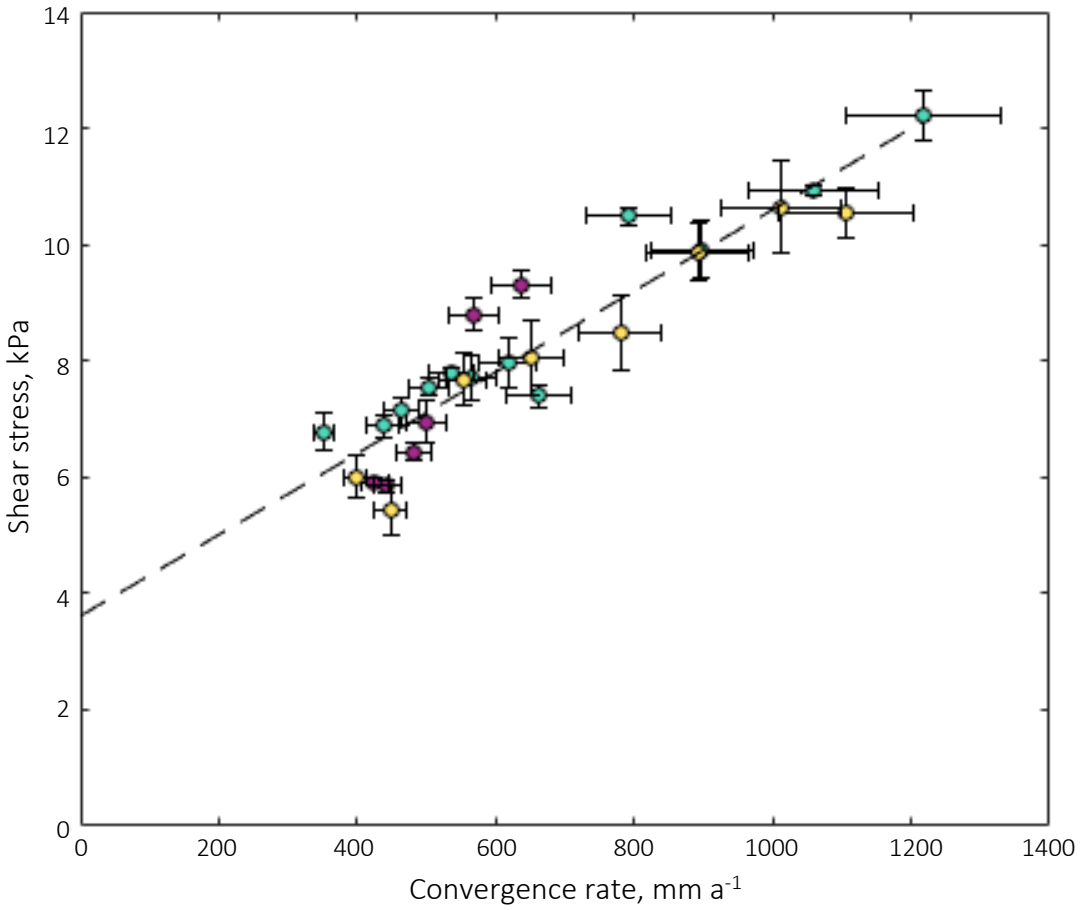

Figure 3.2. Shear stress as a function of convergence rate in the first (pink), third (green), and fourth (yellow) experiments. Error bars indicate one standard deviation. Regression line (see text) is fit with least squares method. A linear fit of these data intersects the y-axis at 3.6 kPa.

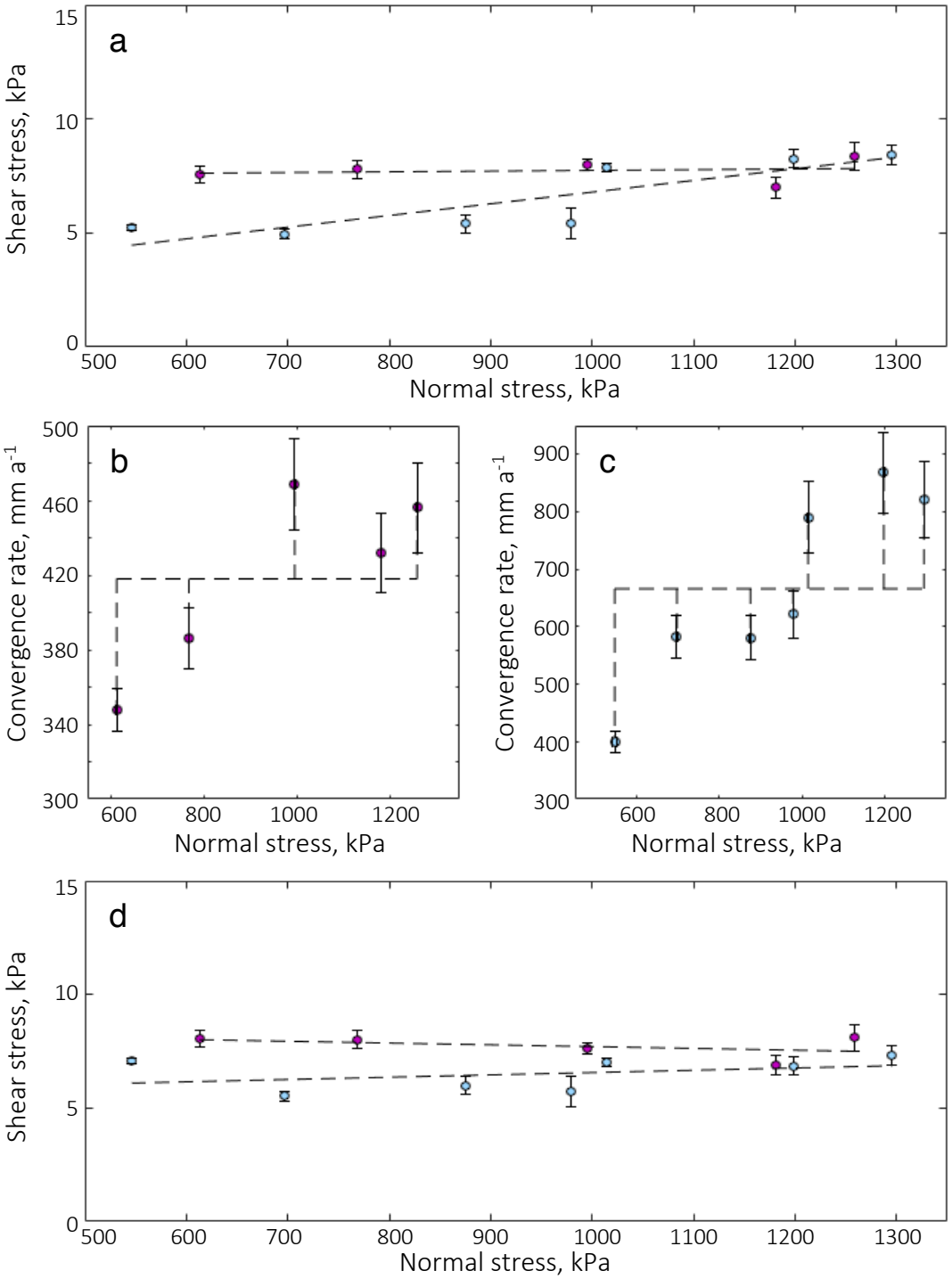

Figure 3.3. (a) Shear stress as a function of normal stress in the first (pink) and second (blue) experiments. The bulk friction coefficients between the ice ring and the bed are 0.0003 and 0.0049. (b, c) Convergence rate and normal stress are codependent in experiments 1 and 2. The convergence rate in excess of the average is illustrated by the vertical dashed lines. (d) Corrected shear stress is plotted as a function of normal stress. Error bars in all plots are one standard deviation. Horizontal error bars are too small to be visible.

Furthermore, any proportionality between normal and shear stress reflects, to some extent, the co-dependence of normal stress and convergence rate. By increasing the normal stress, the pressure-melting temperature decreases and causes the melt rate to increase by steepening thermal gradients in the walls of the ice chamber. Indeed, higher normal stresses corresponded with higher convergence rates (Figs. 3.3b, 3.3c). This codependence was accounted for by subtracting the shear stress associated with any convergence rate observed in excess of its average. Shear stress was computed from the excess convergence rate by using the relationship from the experiments in which convergence rate was varied (Fig. 3.2). After accounting for the co-dependence, there is no significant relationship between normal stress and shear stress (Fig. 3.3d).

Till particles

At the end of an experiment, the ice ring was removed from the chamber as quickly as possible to view the surface that had been in contact with the rock bed. Most particles either 1) fell out of ice when it was lifted off the bed, indicating that ice had not been supporting them from below, or 2) remained in the ice with evidence of cavities that had formed between them and the bed (Fig. 3.4). Thus, cavity formation between rock particles and the bed was prevalent in all experiments, despite all of them ending after a period of high normal stress near 1000 kPa. Furthermore, there was no evidence of bubbly, texturally distinct regelation ice beneath particles. The size and extent of cavities varied widely across experiments, as did the time delay between the end of an experiment and viewing the base of the ice. Unsurprisingly, ice rings that took longer to remove underwent more melting at their bases during removal, so that sizes and shapes of cavities were poorly defined.

As noted in the previous chapter, the medium and large particles (16 and 24 mm diameter) in Experiment 4 were marked with an X on their surfaces where they contacted the

bed. Lines were traced on particles in a plane parallel to the bed. In their final positions after the experiment, the position of the marked original points of contact and the orientation of the originally bed-parallel lines on particles revealed particle rotation (Fig. 3.5). Of the 55 particles in the ice ring at the end of the experiment, 44 did not appear to have rotated, although rotations of less than ~10° were not resolvable. At least eight particles clearly did rotate. While most of these rotated between 25° and 45° (assuming no multiple rotations), one rotated ~70°.

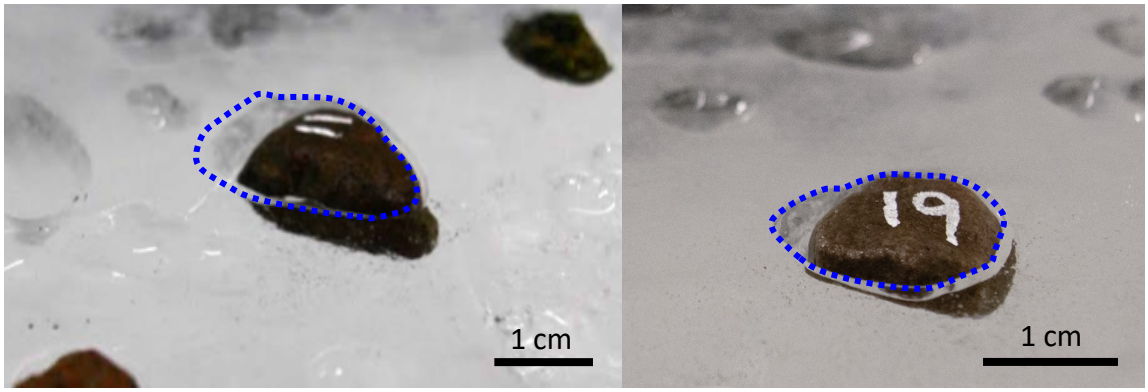

Figure 3.4. Examples of cavities that have formed beneath particles. These photos show the base of an ice ring at the end of an experiment. The smooth ice surface was in contact with the rock bed, and the cavities were filled with water. The blue dotted lines trace the edges of the cavities to clarify their shape. Ice slip was from right to left.

Sliding particles also left striations on the rock bed. While many were thin and shallow, making them difficult to identify, several large striations were up to 1 mm wide and 30 μm deep (the depths of only a few were measured with a white light interferometer, so it is possible that others were deeper). The deeper striations that could be traced were tens of centimeters long, marking most of a particle's displacement in an experiment. Thin cracks formed on the bed surface along mineral foliation throughout the experiments. Striation size and concentration increased noticeably around the largest crack that fractured the bed (Fig. 3.6). Another cluster of faint striations was noticeable around a much smaller surface crack. Cumulative striations faded

with distance from the cracks and were very sparse on the side of the bed where there the surface was well preserved. The particles were also analyzed for weathering. While a few particles fractured and were replaced in subsequent experiments, there was no discernible difference in particle mass or volume between the first and last experiments.

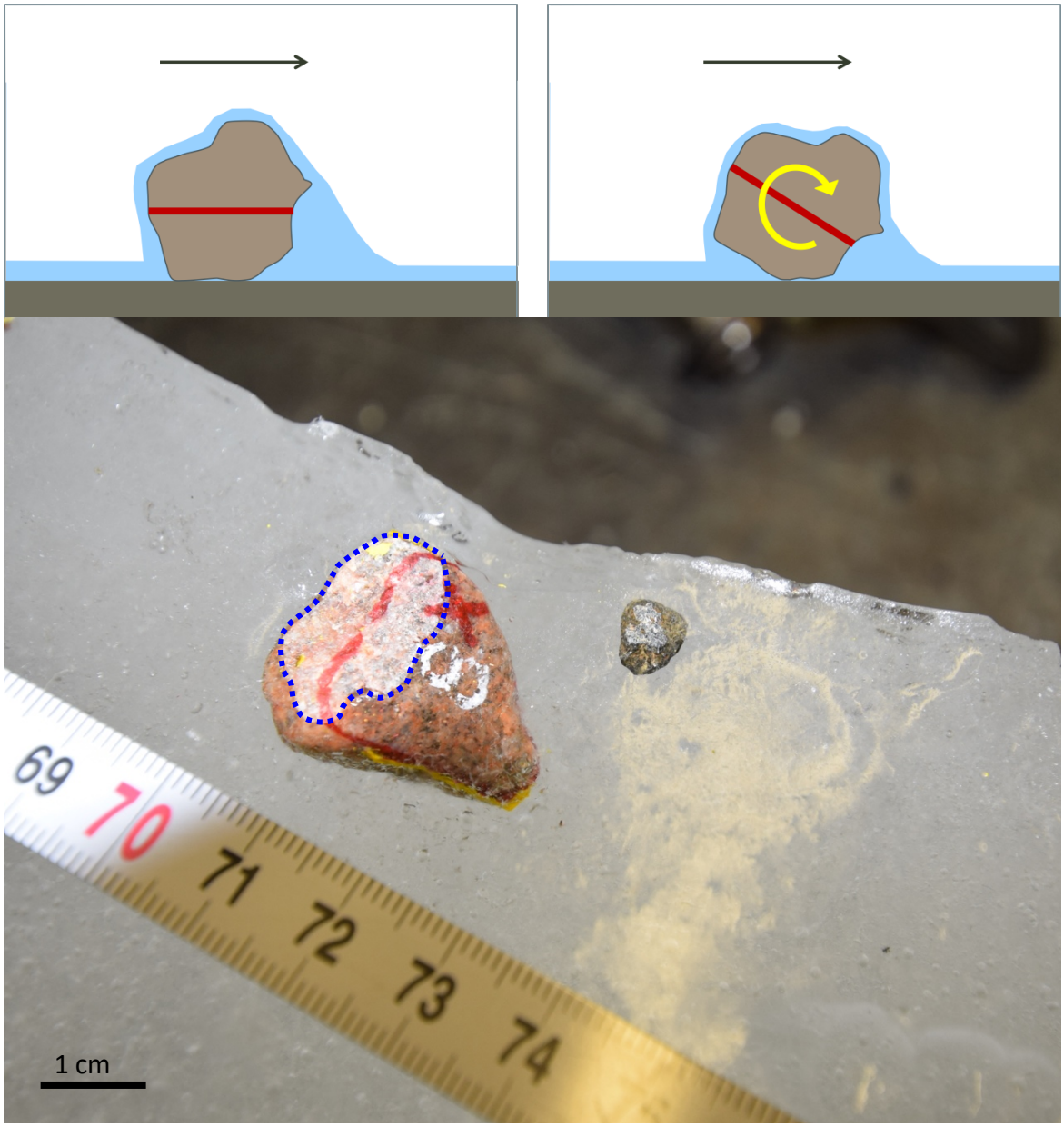

Figure 3.5. A rotated particle at the base of the ice ring at the end of the last experiment. The red line traces a plane that was originally parallel to the bed and the X indicates the original point of contact with the bed. The blue dotted line traces the edge of the ice to show the degree of rotation. Ice slip was from bottom right to upper left.

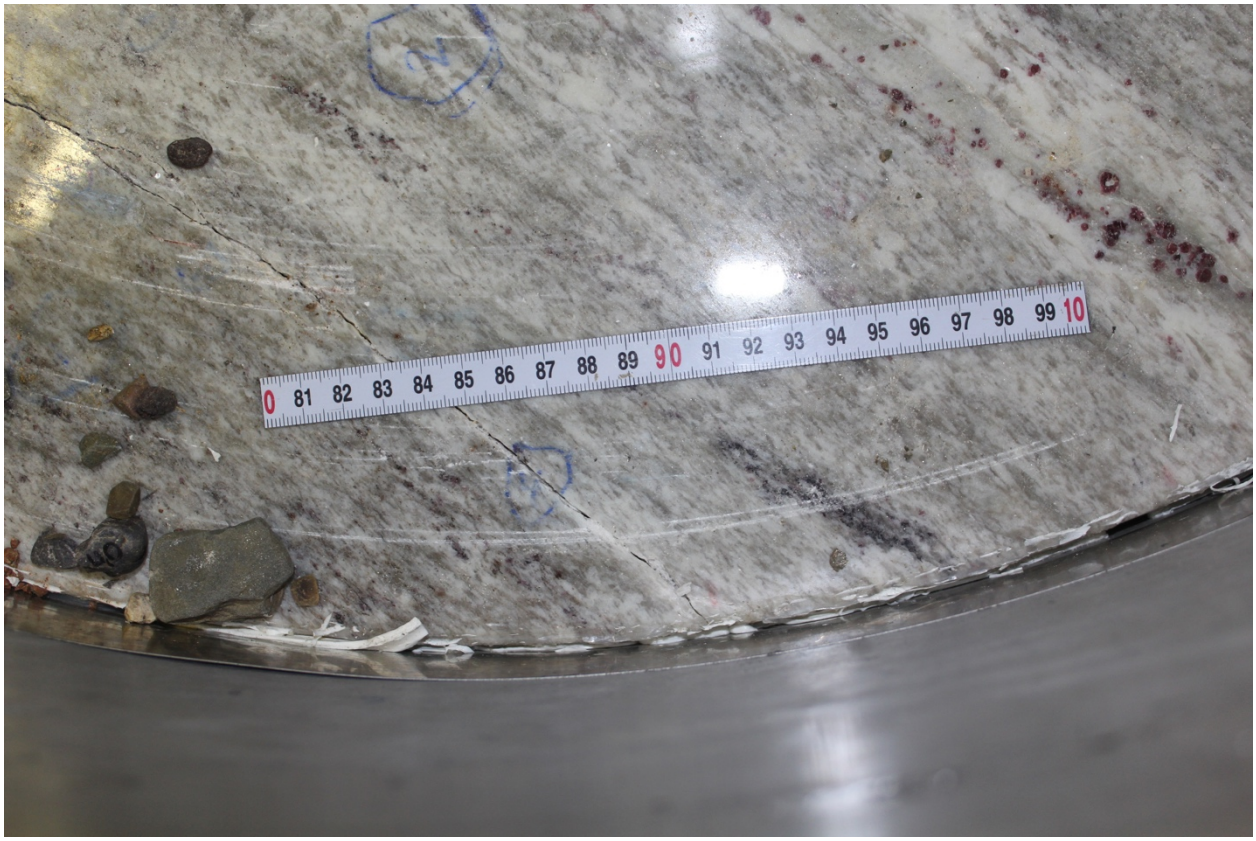

Figure 3.6. Example of striations on the rock bed after the third experiment. Striations were most severe near the crack, which is also visible. Many faint striations in this area and around the bed are not discernable in the photograph. Ice movement was from left to right.

Sliding

In all experiments, ice moved as a plug during slip, with no shear discernable from the initially vertical strings of beads frozen in the ice (Fig. 3.7). Vertical convergence of the ice with the bed created kinks in the bead string, but its final top and bottom positions were not horizontally offset. Nearly all movement, therefore, was accommodated by ice sliding. Displacement of the beads matched the displacement of the toothed upper platen.

Owing to the negligible influence of normal stress on the measured shear stress in these experiments, the melt film thickness between the ice ring and the bed can be estimated from the basal melt rate and by assuming that the melt film supports the full vertical stress on the ice ring.

Under the most common conditions of these experiments when normal stress is maintained near 980 kPa, film thickness is expected to be ~1.3 μm (N. Iverson, pers. comm.).

The estimated thickness of the melt film can be compared to the size of asperities on the rock bed to determine whether the asperities introduce resistance to sliding. A white light interferometer (Zygo Profilometer 7100) was used to analyze the micro-roughness of the bed. The analysis from several striation-free locations on the bed revealed a flat surface with relatively deep pockets where less resistant crystals had weathered out (Fig. 3.8). The heights of asperities on the flat surface are well under one μm, but the pockets are as deep as 13 μm.

During each experiment, the ice was slid at a constant speed of 7.6 m a^{-1} at the radial centerline of the ice ring for up to 25 days. Particle displacements were compared to ice displacement in the first experiment by referencing photographs taken before and after. Several of the particles came out with the ice ring or could not be found, but the paths of nine were reasonably identifiable (Fig. 3.9). The average displacement of the nine particles (five small, one medium, three large) was 86% ± 5% of the ice displacement. These particles were slowed by the friction between them and the bed while ice moved longitudinally around them. Whether they moved at a constant speed like the ice ring could not be measured but is unlikely owing to the temporal variability of shear stresses supported by clasts during experiments.

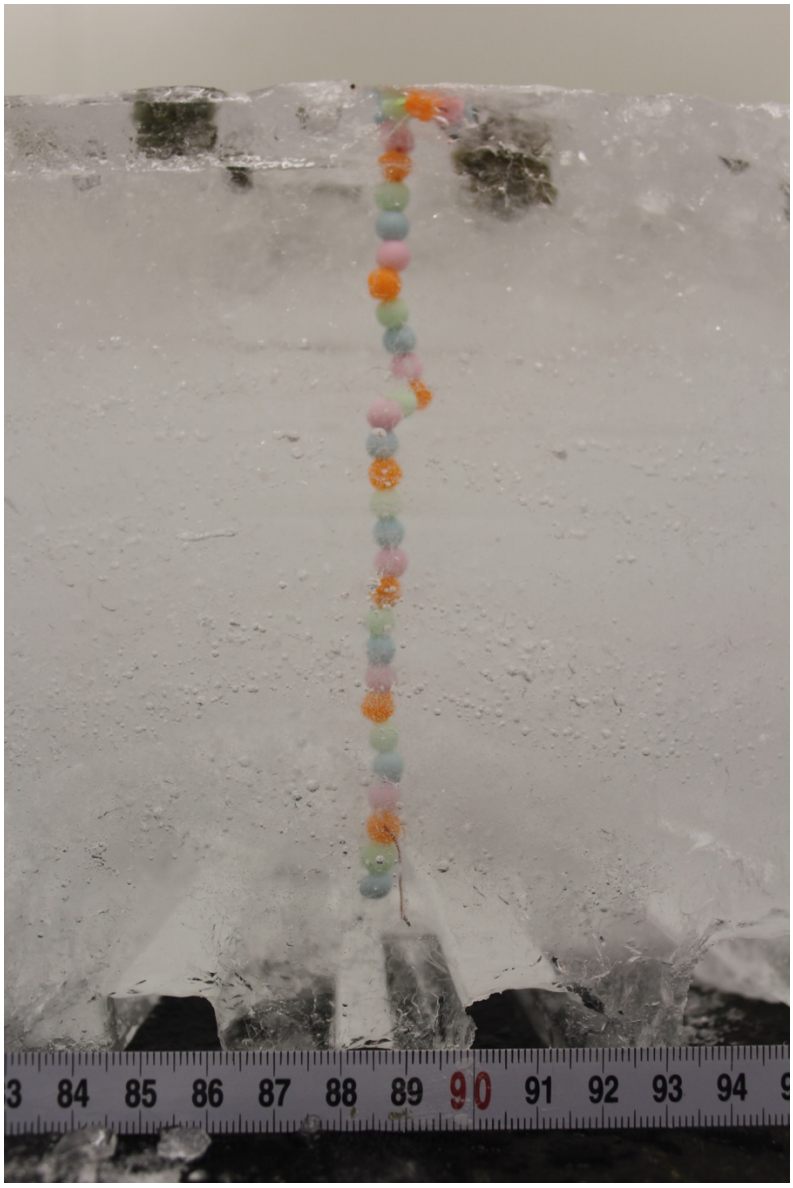

Figure 3.7. Photo of a representative bead string in an ice ring resting upside-down at the end of Experiment 3. Ice slip was from right to left.

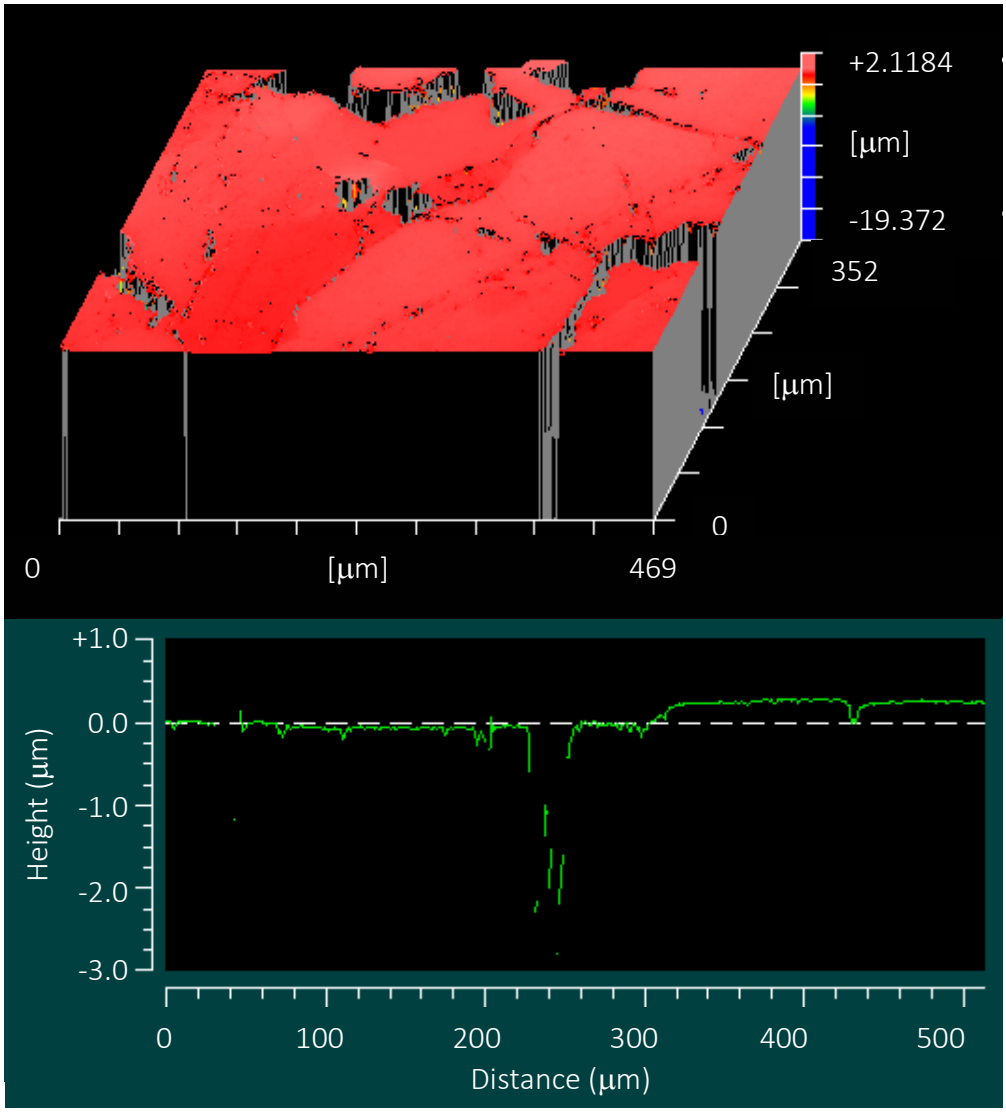

Figure 3.8. An example topographic transect of the polished rock slab, displayed on the Zygo 7100 Profilometer software interface.

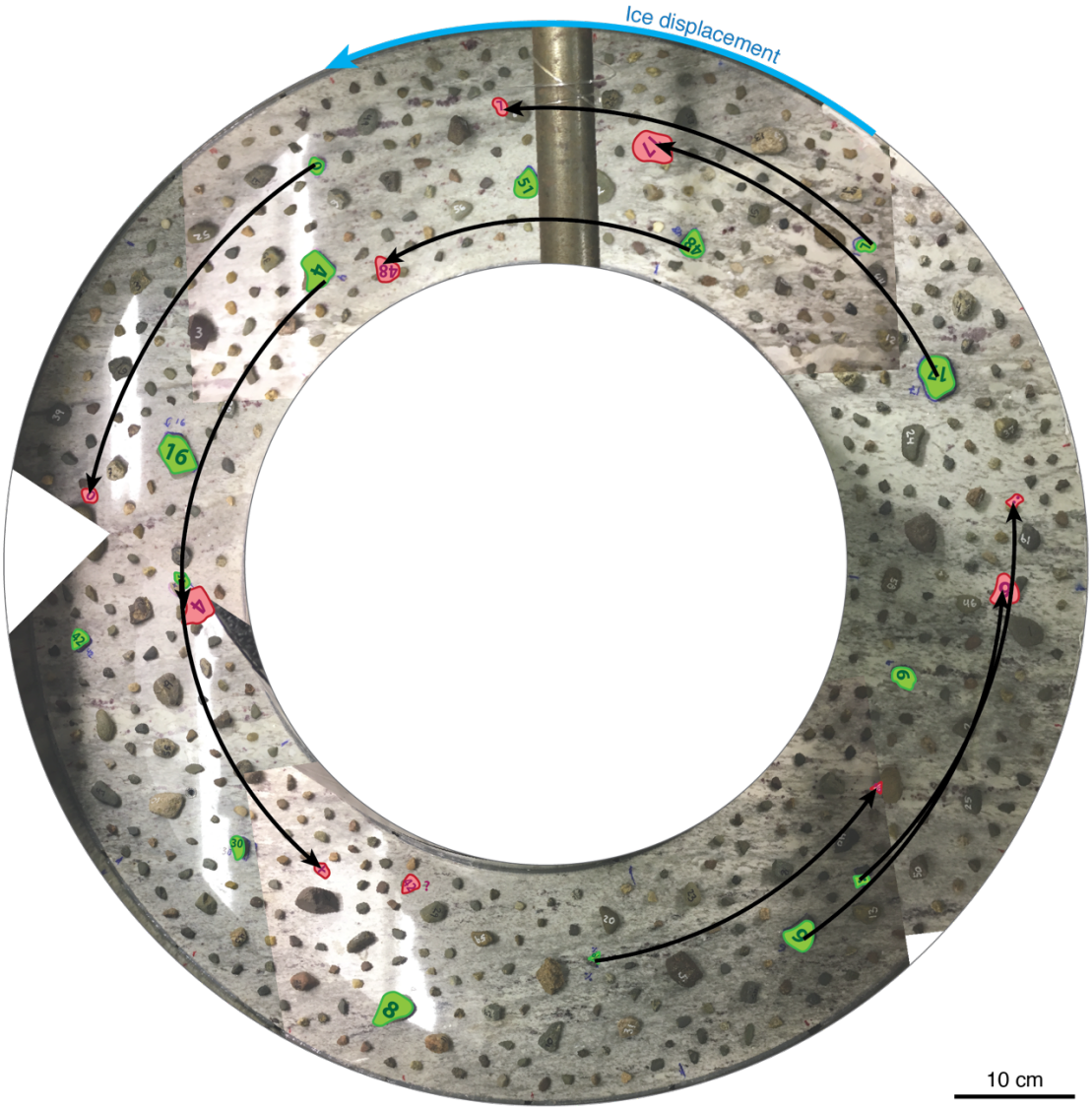

Figure 3.9. Particle displacement in Experiment 1. Starting positions are traced in green and final positions are traced in red. Black arrows trace the assumed path, along which displacement was measured. Ice displacement at the outer edge of the ice ring is illustrated in blue for comparison.

CHAPTER 4. DISCUSSION

Assumptions

Interpreting our results requires first ruling out intermolecular interactions associated with premelting, a condition which enables liquid films to exist below the pressure-melting temperature, and which may disrupt the vertical force balance on particles in ice and the thickness of melt films at the pressure-melting temperature. Following the logic outlined by Emerson and Rempel (2007), these forces can be neglected in the context of these experiments because

$$\lambda \ll \left(\frac{3d^2\eta_w\dot{m}}{L}\right)^{1/3} , \tag{4.1}$$

where λ is a length scale that characterizes the strength of the intermolecular forces that cause premelting and is equal to 0.5 nm (Wettlaufer and Worster, 1995; Emerson and Rempel, 2007). The particle diameter is d, η_w is the dynamic viscosity of water, $\dot{m}$ is the melt rate (equivalent to convergence rate of ice with the bed, v_n), and L is the volumetric latent heat of fusion ($3.1\text{x}10^8$ J m^{-3}). Using the minimum convergence rate measured in these experiments ($1.1\text{x}10^{-8}$ m s^{-1}) and considering the smallest particle size (8 mm diameter), the right-hand side of the inequality was never less than 15 nm is these experiments, and hence was much larger than λ.

The following discussion also ignores the insubstantial contribution of the buoyant weights of particles to shear stress. The shear-stress component due to buoyant weight scales with R^3 and is calculated to be three orders of magnitude smaller than the shear stress measured in our experiments, owing to the small particles used in the experiments.

Comparison with Boulton's theoretical model

Cavities observed in our experiments and other experiments (Iverson, 1990, 1993; Byers et al., 2012; Hansen and Zoet, 2020) offer a potential explanation for the independence of shear

stress and ice normal stress that contradicts Boulton's theory (Boulton, 1974). These cavities were observed beneath and on the lee sides of particles in contact with the bed where water did not refreeze as regelation ice (Fig. 3.4). In addition to the pressure gradient in the ice associated with ice flow past particles, these cavities were maintained by high water pressure, heat flow from the bed and frictional heating at particle-bed contacts.

To sustain a steady-state cavity, the water pressure in the cavity must at least slightly exceed the pressure in the melt film between ice and the bed in areas adjacent to particles. For a cavity of unchanging size, any water produced on the perimeter of a particle has to be driven into the melt film between the ice and the bed. Thus, water pressure in the cavity must be greater than water pressure in the melt film, which equals the ice pressure there. As a result, increases in normal stress on the ice must be accompanied by increases in cavity water pressure in order for drainage to satisfy mass conservation. Resultant increases in water pressure in cavities counteract increases in normal force on the upper surfaces of particles so that contact force between a particle and the bed remains unchanged with changes in ice normal stress on the bed (Fig. 4.1).

If drainage near particles is not restricted exclusively to flow in the melt film, water can drain downward through the bed and water pressure in cavities may not be sufficient to counteract the influence of ice pressure on particle-bed contact force. Striation depth and width, proportional to particle-bed contact force, were much greater near a large crack in the bed that introduced a near-field, vertical drainage path in our experiments (Fig. 3.6). Striations were also more prominent near smaller cracks and the edges of the bed. In natural settings, proximity to drainage channels, bedrock topography that causes ice-bed separation, and bed permeability, either from fractures or pervasively at grain scales, can introduce similar easy drainage

opportunities. However, a bed without easy drainage over lengths of the order of particle sizes is probably the best null hypothesis.

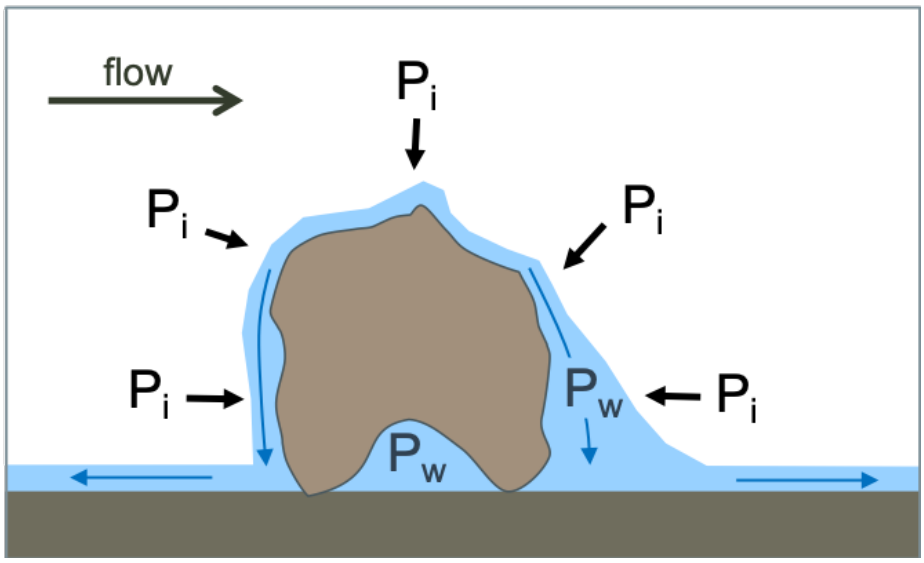

Figure 4.1. Schematic of ice pressure and water pressure near a particle in contact with the bed. As ice melts, meltwater is produced at the interface between the particle and ice, drains through the cavity along the lower surface of the particle, and then along the bed to its edges. Drainage discharge is limited by the thickness of the melt film and the pressure gradient in the film.

The relationship between shear stress and normal stress observed by Hansen and Zoet (2020) is likely related to easy drainage in their experiments. In their experiments, drainage holes (< 4 mm) were drilled into the bed within ~2 cm of rock particles. This proximity to drainage holes may have kept high water pressure from being maintained in the cavities so that particle-bed contact force depended on the overburden ice pressure. Small cavities were observed in the lee of clasts but were not a dominant feature in the experiments (Hansen and Zoet, 2020), consistent with low water pressure beneath particles. The same explanation can be applied to the debris-bed friction experiments conducted by Zoet et al. (2013), in which a dependence on normal stress was recorded; water flowed through the melt film over a maximum distance of only 2.5 cm before draining to atmospheric pressure. Natural subglacial conditions are unlikely

to be uniformly well-drained if the bed is impermeable. Instead, debris-bed drag that depends on normal stress is likely only concentrated locally around features like drainage channels and fractures.

Comparison with Hallet's theoretical model

Our results clearly do not support Boulton's theory; rather they support that shear stress is controlled by convergence rate, as Hallet anticipated. The shear stress, τ_d, predicted by his theoretical model (Hallet, 1981), can be calculated using the conditions of the experiments and summed across each of the three size categories:

$$\tau_d = \sum_{i=1}^{3} \mu \left(\frac{f 4\pi \eta_i R_i^3}{R_*^2 + R_i^2} \right) v_n c_i \ , \tag{4.2}$$

where the friction coefficient between rock particles and the rock platen, μ, is 0.37 (determined in the aforementioned rock-friction tests). The convergence rate of ice towards the bed, v_n, is due to only melting in our experiments, c is the number of particles of each size used in the experiments (463, 62, and 19), and R is the particle radius (4 mm, 8 mm, and 12 mm). The bed-influence factor $f = 2.4$, is based on Hallet (1981) and Byers et al. (2012). The effective ice viscosity is η, and R^* is the threshold particle size for which ice moving around rock particles by enhanced ice creep and regelation contribute equally to the drag.

To determine η, we define x as parallel to the local bed surface in the direction of sliding y as normal to it, and v as the ice velocity in the y direction toward the bed. Consider the definitions of shear stress for a linear-viscous fluid,

$$\tau_{xy} = \eta \frac{dv}{dx} \ , \tag{4.3}$$

shear strain rate of the ice,

$$\dot{\varepsilon}_{xy} = \frac{1}{2} \frac{dv}{dx} \ , \tag{4.4}$$

and Glen's Flow Law,

$$\tau_{xy} = \left(\frac{\dot{\varepsilon}_{xy}}{A}\right)^{1/n}, \tag{4.5}$$

where A is a fluidity parameter for ice and sometimes called the pre-factor in the flow law (Cuffey and Paterson, 2010). In combination, Equations 4.3-4.5 can be rearranged to write the effective ice viscosity as

$$\eta = \frac{\dot{\varepsilon}_{xy}^{\left(\frac{1}{n}-1\right)}}{2A^{\frac{1}{n}}}. \tag{4.6}$$

We estimate strain rate, $\dot{\varepsilon}_{xy}$, by assuming that the radius of the cavity around a particle is no more than two times greater than the radius of the particle itself. We also assume that the magnitude of change in v from the top to the bottom of the particle is defined by a constant k ($\leq$ 1.0). Following these assumptions, strain rate is written as,

$$\dot{\varepsilon}_{xy} = \frac{kv}{4R}. \tag{4.7}$$

Equation 4.7 can be substituted into Equation 4.6, so that effective ice viscosity can be written in terms of the flow law parameters for ice and convergence rate:

$$\eta = \frac{(kv_n/4R)^{(1/n-1)}}{2A^{1/n}}. \tag{4.8}$$

The stress exponent, n, in the flow law, and the fluidity parameter, A, are assumed to be 3 and $2.4\text{x}10^{-24}$ s^{-1} Pa^{-3}, respectively (Cuffey and Paterson, 2010), and $k = 0.9$ is used because it yields close to a maximum value for the reference strain rate, $\dot{\varepsilon}_{xy}$, assuming $v_n > 0$ at the very tops of particles.

Watts derived an expression for the threshold particle size,

$$R^* = \left(\frac{3\eta c}{L\rho_s}\right)^{1/2}. \tag{4.9}$$

The relevant parameters are the melting point depression with pressure, c (7.4×10^{-8} °C Pa^{-1}), the volumetric latent heat, L (3.1×10^{8} J m^{-3}), and the rock/ice resistivity parameter, ρ_s (0.179 m °C W^{-1}), which is the inverse of the average thermal conductivity of the ice and rock particles.

The shear stress calculated from this model (Equation 4.2) overpredicts the shear stress for the range of convergence rates used in these experiments (Fig. 4.2a). Importantly, Hallet's model may not be appropriate for particles in close proximity to the bed because the bed may prevent refreezing during regelation. Hallet's model is founded on particle-bed contact force being driven by the movement of ice flowing around particles in contact with the bed (Fig. 4.2c). For the particle sizes used in these experiments, regelation is expected to be the dominant mechanism of ice movement past them. The drag coefficient in Hallet's model contains this assumption (Hallet, 1981), but regelation ice was conspicuously absent at the end of the experiments. This observation likely reflects that the bed is a source of heat, which prevents refreezing of meltwater (Iverson, 1990), and necessitates an alternative model.

Emerson and Rempel model

Emerson and Rempel (2007) explained particle-bed contact force by appealing to the need for mass conservation within the melt film surrounding particles. Assuming that heat conduction from the bed and upward through particles is not significantly impaired by water in the narrow spaces where cavities exist beneath particles, the melt rate at the upper surface of a particle is approximately equal to the far-field melt rate at the ice-bed interface. Melting ice at a particle's upper surface produces a flux of water that flows through the ice-particle melt film from the top of a particle, through the underlying cavity, and outward to the edge of the bed where water is allowed to drain to atmospheric pressure. Increasing ice-bed convergence rate through basal melting increases the flux of water in the melt film, steepening the water-pressure

gradient in the melt film at the ice-particle interface. The water-pressure gradient results in the downward drag on the particle, which equals the resultant particle-bed contact force (Fig. 4.2d). Thus, an increase in ice-bed convergence rate through an increase in basal melting causes an increase in contact force.

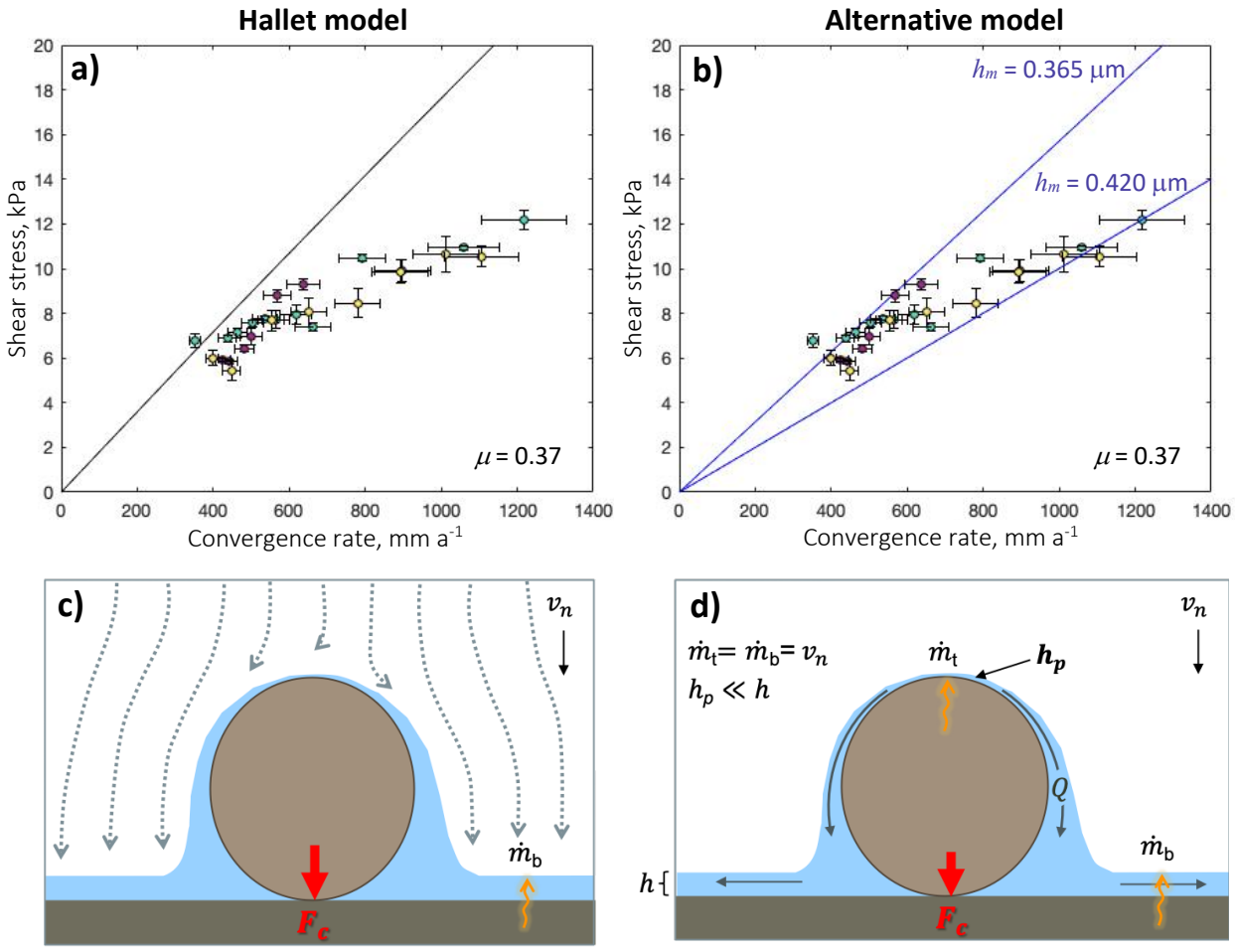

Figure 4.2. (a) Shear stress calculated by Hallet's model using the conditions of our experiments where $\mu = 0.37$ and $k = 0.9$. The non-linearity resulting from changing effective ice viscosity is imperceptible. (b) Shear stress calculated with the adjusted model, derived from Emerson and Rempel (2007), using two example film thicknesses above medium size particles. (c) Schematic illustrating that the source of drag in Hallet's model is the movement of ice around a particle in contact with the bed. (d) Schematic illustrating that the source of drag in the alternative model is the flow of water through the melt film.

In this case, particle-bed contact force is

$$F_c = \left(\frac{4\pi R^4 \eta_w \dot{m}}{{h_p}^3}\right), \tag{4.10}$$

where v_n is equated with the basal melt rate, $\dot{m}$, and η_w is the viscosity of water (Emerson and Rempel, 2007). Assumed in the derivation of this equation is that the far-field film thickness, h, is much smaller than particle diameter and that the film thickness above particles, h_p, is much smaller than the far-field film thickness and particle radius. This alternative expression for contact force can replace Hallet's expression (Equation 1.3) so that debris-bed friction can be considered in the absence of regelation:

$$\tau_d = \mu \left(\frac{4\pi\eta_w R^4}{{h_p}^3}\right) v_n c\,. \tag{4.11}$$

The thicknesses of melt films above particles is not known in these experiments, so h_p is used as a fitting parameter, with the value for the medium-sized clasts used as a reference. The thicknesses of melt films above differently sized particles are scaled accordingly, assuming that because melting along larger surface areas produces greater fluxes of water, melt films are thicker above larger particles so that that h_p is proportional to R. This assumption yields the following relation for τ_d that pertains specifically to these experiments with three particle sizes:

$$\tau_d = \mu 4\pi\eta_w v_n \sum_{i=1}^{3} \frac{{R_i}^4 c_i}{\left(\frac{h_m R_i}{R_m}\right)^3}\ . \tag{4.12}$$

The radius of medium particles is R_m, and the film thickness above them is h_m.

Figure 4.2b shows results of this alternative model, compared with experimental data using two possible film thicknesses for medium-sized clasts: 0.365 and 0.420 μm. These values of h_m fulfill the criteria that they be substantially smaller than both the particle radii and the far-field thickness of the melt film between ice and the bed (~1.3 μm). Although the two values

produce results that largely bracket the data, neither film thickness alone provides a good fit to the data. In particular, Equation 4.12 over-predicts the sensitivity of debris-bed friction to convergence rate.

Particle rotation

Particle rotation was observed in our experiments and in experiments by others (Iverson, 1990), but is neglected in both models for debris-bed friction presented thus far (Equations 4.2 and 4.12), despite the potential for rotation limiting friction between particles and the bed to values less than those indicated by the rock-to-rock friction coefficient ($\mu = 0.37$). Particle rotation is controlled by the torque on particles, which depends on particle-bed contact force, and equals $\mu F_c R$. These experiments demonstrate that particle-bed contact force depends on convergence rate (Fig. 3.2). Therefore, higher convergence rates will cause a greater tendency for particle rotation, reducing the shear force supported at particle-bed contacts to values limited not by the measured rock-to-rock friction coefficient but by the smaller "effective" friction coefficient required to rotate particles.

Decreasing the effective friction coefficient from the measured dynamic particle-bed friction coefficient of 0.37 would decrease the sensitivity of debris-bed friction to convergence rate (i.e., the slope of the modeled curves) (Figs. 4.2a and 4.2b). Considering the inverse relationship between convergence rate and effective friction coefficient, the effective friction coefficient may continuously decrease and reduce the slope of the curve with increasing convergence rate. A decreasing effective friction coefficient can allow the model to better fit the experimental data. Figure 4.3 illustrates a scenario in which particle rotation decreases the effective friction coefficient, μ_{eff}, linearly with increasing convergence rate. The effective friction coefficient is 0.20 when convergence rate reaches 1400 mm a^{-1}, and film thickness above

medium-sized particles is 0.27 µm. Unfortunately, the reduction in μ_{eff} with increasing convergence rate and particle rotation cannot be independently estimated quantitatively without assessing the ice drag on the angularities of particles that resists their rotation—a task beyond the scope of this thesis.

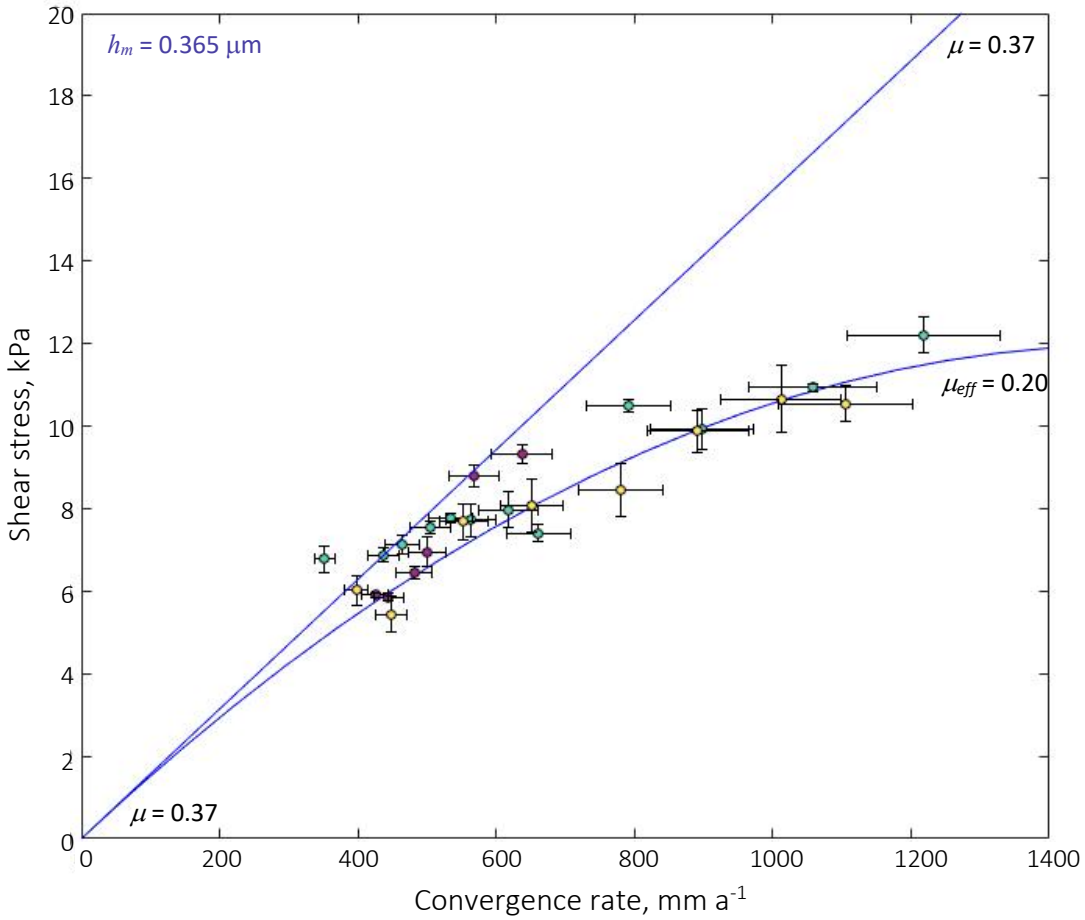

Figure 4.3. Shear stress calculated with the adjusted model, with and without a changing effective friction coefficient in response to rolling particles. The straight line illustrates a constant rock-to-rock friction coefficient, 0.37, consistent with the ancillary experiments with sliding clasts in an epoxy slab. The curved line illustrates the effective friction coefficient decreasing steadily from 0.37 at convergence rate = 0 mm a^{-1} to 0.20 at convergence rate = 1400 mm a^{-1}. Film thickness above medium-sized particles in all calculations is 0.27 µm.

Particle properties

Particle-bed friction is, in part, controlled by the angularity and hardness of particles. Granite particles used in experiments by Iverson et al. (1990) and Hansen and Zoet (2020) were

highly angular, which increases debris-bed friction in two ways: angularities reduce the tendency for particle rotation, and they allow particles to striate the bed more deeply, increasing rock-to-rock friction (Iverson, 1991). Additionally, the beds in these other two sets of experiments were composed of marble and limestone, respectively. These rocks are softer than granite, allowing deeper scratching of the bed and higher associated rock-to-rock friction coefficients. This effect probably explains the rock-to-rock friction coefficient in the Hanson and Zoet (2020) study (0.72) that is higher than that measured in the ancillary rock friction experiments described herein (0.37). Most commonly, glacial debris is sourced from the bed and would thus not have a large hardness contrast with the bed. Our experiments were designed so that particles and the bed were crystalline rock of similar hardness. The particles were sourced from natural till, so their angularity was appropriate and less than that of earlier experiments (Fig. 2.5 vs. Fig. 3e in Hansen and Zoet (2020)).

Particles were separated from one another in experiments because drag forces on clustered particles cannot be readily the theory of Watts (1974), as used by Hallet (1979; 1981). Closely spaced particles can result in a situation in which the rate of ice motion downward past the particles is exceeded by the basal melt rate. This opens up a macroscopic continuous cavity beneath the particle array (Iverson, 1993). A continuous cavity can mean that the water pressure beneath rock particles reflects the water pressure in the subglacial hydraulic system because the cavity allows direct, non-diffusive hydraulic communication with big linked cavities and channels. Because water pressure in subglacial drainage systems is usually much lower than the high confined water pressure of an isolated cavity beneath an individual particle, effective normal stress may influence particle-bed contact force when particles are clustered.

Even if particles are not closely spaced, there is a point at which particle concentration can make debris-bed friction dependent on normal stress. Emerson and Rempel (2007) found that debris-bed friction responded differently to normal stress variations in ice with relatively high and low particle concentrations. Their explanation is that at low concentrations, the melt film above particles is thick enough so that only a small fraction of the normal load is transferred to particle-bed contacts. At high concentrations, the melt films are thinner, requiring steeper water-pressure gradients to drive the flow in films and resulting in high enough water pressure to transfer more of the normal stress on the ice to particles (Emerson and Rempel, 2007). Both particle clustering and concentration are subject to change over time as particles moving at different speeds rearrange themselves relative to one another and as more particles are introduced to the bed by melting out of the ice or produced by erosion of the bed.

Finally, there is likely an upper and lower particle size limit for which these relationships are applicable. Realistically, there will be many particles at glacier beds that are much smaller than in these experiments (e.g., sand, silt). As Emerson and Rempel demonstrated experimentally (2007), particles may not contribute to debris-bed friction as they approach the size of the melt film and become fully drowned in it. Conversely, there is almost certainly an upper particle size limit for which water flow through the melt film can no longer contribute significant downward drag. Ice movement around particles greater than ~0.11 m is dominated by enhanced ice deformation as opposed to regelation, at which point the applicability of Hallet's model could be reevaluated.

Sliding speed

Particles moved at close to the speed of basal ice (Fig. 3.9), indicating that they were in light contact with the bed as Hallet anticipated (Hallet, 1979, 1981). The relative bed-parallel velocity between particles and basal ice could be estimated using Hallet's equation for the drag

force on particles (Equation 1.3), but by applying it to ice flow past particles parallel to the local bed slope, rather than normal to it. The equation could be modified for bed-parallel flow by excluding the bed influence factor, f, or changing its value to account for the bed's effect on bed-parallel flow and neglecting the small buoyant weights of particles. Calculating the bed-parallel drag force by dividing the measured shear stress, τ_d, by the areal concentration of particles, would allow the relative velocity of ice past particles to be calculated using the drag coefficient of Equation 1.3. Absolute particle velocity could be found by subtracting the relative velocity from the sliding velocity of the ice ring. Although there are sufficient data for these calculations, application of Hallet's equation to bed-parallel flow past particles would not be well-motivated because there was no evidence of regelation ice in these experiments.

Debris-bed friction is expected to increase with sliding speed because of the increased rate of ice convergence toward the stoss surfaces of bumps on the bed that is expected as sliding speed increases. However, this effect may be negated by decreased areas of contact between ice and stoss surfaces as sliding speed increases (Iverson et al., 2020). Water-filled cavities on the lee sides of bedrock bumps grow when sliding speed increases and partly drown stoss surfaces, highlighting that estimating debris-bed friction beneath glaciers requires more than accurately estimating the particle-bed contact forces that are the focus of this thesis.

Temperature control

The clean-ice friction coefficient measured in our experiments is lower than that measured in other experiments with clean ice (McCarthy et al., 2017), which likely reflects differences in the control of ice temperature. In McCarthy's experiments, the reported ice-rock friction coefficients at the pressure-melting temperature was 0.035, which is an order of magnitude greater than the clean-ice friction coefficient recorded in our experiments. Because

their temperature measurements have an error of ±1.8ºC (McCarthy et al., 2017), the higher friction coefficient was probably a result of their ice being below the pressure-melting temperature. We are confident that our experiments were conducted at the pressure-melting temperature because of our substantially more precise temperature control and measurements (±0.01ºC).

Although drainage conditions, as noted, affect differences between our results and those of Hansen and Zoet (2020), ice temperature is also a distinguishing factor. Ice was melting at the ice-rock interface in their experiments, but a vertical temperature gradient resulted in the ice being below the pressure-melting temperature adjacent to particles within one centimeter of the bed. This “cold” ice required an analysis that is different from those herein, owing to the need to address the effect of much thinner melt films at particle surfaces associated with premelting. This cold ice contributed to higher contact forces than if ice in those experiments had been fully at the pressure-melting temperature.

CHAPTER 5. CONCLUSION

These experiments more closely simulate subglacial conditions than previous sliding experiments with debris in ice. Most importantly, ice everywhere is kept at the pressure-melting temperature, and water produced by melting moves along the bed over length scales that are significantly larger than clast diameters before draining to atmospheric pressure. Meeting these conditions has a major influence on contact forces and friction. Also important is that a large number of particles is considered. The range of convergence rates considered is appropriate for the stoss surfaces of a glacier bed, and the sliding speed is sufficiently small to be realistic. Particles are sourced from till that is crystalline like the bed, so particles have appropriate angularity and relative hardness with the bed.

Clean-ice experiments confirm that friction between smooth rock and ice at the pressure-melting temperature is negligible if drainage conditions promote a sufficiently thick water film at the bed. This observation supports a fundamental assumption of clean-ice sliding theories (e.g., Weertman, 1957; Lliboutry, 1968; Nye, 1970). Recent experiments that indicated significant friction coefficients between clean ice and rock were likely conducted below the pressure-melting temperature (McCarthy et al., 2017).

Debris-bed friction is independent of the normal stress that ice exerts on the bed. Easy drainage through the bed and closely spaced particles likely make debris-bed shear stresses more susceptible to normal stress, but these conditions are not likely to be generally applicable. Previous experiments indicating dependence of debris-bed shear stresses on normal stress have been below the pressure-melting temperature (Hansen and Zoet, 2020), had drainage to atmospheric pressure near particle-bed contacts (Zoet et al., 2013; Hansen and Zoet, 2020), or had high particle concentrations (Emerson and Rempel, 2007).

As Hallet (1979; 1981) anticipated, debris-bed friction depends on the convergence rate of ice with the bed. However, his model does a poor job predicting particle-bed contact forces. Moreover, although in his model regelation is the principle mechanism by which ice flows past particles, there is no evidence of regelation ice between particles and the bed in this study or any other study. An alternative model for particle-bed contact force, in which the bed-normal drag on particles depends on the water-pressure gradient in films surrounding particles, is more appropriate. It can better fit the data if particle rotations and their impact on effective particle-bed friction coefficients is considered.

Future studies can refine the results of these experiments by better isolating effects of variables that are not adequately explored in this thesis. Experiments with fine particles that are not much larger than the melt film are warranted to test whether there is a minimum particle-size limit for debris-bed friction to be significant. The use of beds with substantial and varying permeabilities would provide a test of the connection between water pressure around particles and a dependence on normal stress. Particles with radically different angularities could be used to test the effects of particle rotation. Finally, the influence of subglacial cavities caused by topography could be studied by replicating these experiments using a bed with decimeter-scale bumps that induce cavities; such experiments with debris in ice, and without debris to isolate drag due to bed roughness, would add realism to the experiments and possibly insight to the problem of debris friction as a source of drag at glacier beds.

REFERENCES

Boulton, G.S., 1974, Processes and patterns of glacial erosion, *in* Coates, D.R. ed., Glacial Geomorphology, Binghamton, New York, State University of New York, Geomorphology, Annual Geomorphology Symposia 5, p. 41–87.

Boulton, G.S., Morris, E.M., Armstrong, A.A., and Thomas, A., 1979, Direct measurement of stress at the base of a glacier: Journal of Glaciology, v. 22, p. 3–24.

Byers, J., Cohen, D., and Iverson, N.R., 2012, Subglacial clast/bed contact forces: Journal of Glaciology, v. 58, p. 89–98, doi:10.3189/2012JoG11J126.

Cohen, D., Iverson, N.R., Hooyer, T.S., Fischer, U.H., Jackson, M., and Moore, P.L., 2005, Debris-bed friction of hard-bedded glaciers: Journal of Geophysical Research, v. 110, p. F02007, doi:10.1029/2004JF000228.

Cuffey, K.M., and Paterson, W.S.B., 2010, The Physics of Glaciers: Academic Press.

DeConto, R.M., and Pollard, D., 2016, Contribution of Antarctica to past and future sea-level rise: Nature, v. 531, p. 591–597.

Egholm, D.L., Nielsen, S.B., Pedersen, V.K., and Lesemann, J.E., 2009, Glacial effects limiting mountain height: Nature, v. 460, p. 884–887.

Emerson, L.F., and Rempel, A.W., 2007, Thresholds in the sliding resistance of simulated basal ice: The Cryosphere, p. 10.

Fowler, A.C., 1981, A theoretical treatment of the sliding of glaciers in the absense of cavitation: Philosophical Transactions of the Royal Society of London. Series A, Mathematical and Physical Sciences, v. 298, p. 637–681.

Gilbert, G.K., 1906, Crescentic gouges on glaciated surfaces: Bulletin of the Geological Society of America, v. 17, p. 303–316.

Gudmundsson, G.H., 1997, Basal-flow characteristics of a non-linear flow sliding frictionless over strongly undulating bedrock: Journal of Glaciology, v. 43, p. 80–89.

Hallet, B., 1979, A theoretical model of glacial abrasion: Journal of Glaciology, v. 23, p. 39–50, doi:10.3189/S0022143000029725.

Hallet, B., 1981, Glacial abrasion and sliding: their dependence on the debris concentration in basal ice: Annals of Glaciology, v. 2, p. 23–28, doi:10.3189/172756481794352487.

Hansen, D.D., and Zoet, L.K., 2020, Experimental constraints on subglacial rock friction: Annals of Glaciology, p. 1–12, doi:10.1017/aog.2019.47.

Headley, R.M., and Ehlers, T.A., 2015, Ice flow models and glacial erosion over multiple glacial-interglacial cycles: Earth Surface Dynamics, v. 3, p. 153.

Herman, F., Beaud, F., Champagnac, J.-D., Lemieux, J.-M., and Sternai, P., 2011, Glacial hydrology and erosion patterns: a mechanism for carving glacial valleys: Earth and Planetary Science Letters, v. 310, p. 498–508.

Hooke, R.L., and Iverson, N.R., 1995, Grain-size distribution in deforming subglacial tills: role of grain fracture: Geology, v. 23, p. 57–60.

IPCC, 2019, IPCC special report on the ocean and cryosphere in a changing climate.:

Iverson, N.R., 1990, Laboratory simulations of glacial abrasion: comparison with theory: Journal of Glaciology, v. 36, p. 304–314, doi:10.3189/002214390793701264.

Iverson, N.R., 1991, Morphology of glacial striae: implications for abrasion of glacier beds and fault surfaces: Geological Society of America Bulletin, v. 103, p. 1308–1316.

Iverson, N.R., 1993, Regelation of ice through debris at glacier beds: implications for sediment transport: Geology, v. 21, p. 559–562, doi:10.1130/0091-7613(1993)021<0559:ROITDA>2.3.CO;2.

Iverson, N.R., 2010, Shear resistance and continuity of subglacial till: hydrology rules: Journal of Glaciology, v. 56, p. 1104–1114.

Iverson, N.R., Cohen, D., Hooyer, T.S., Fischer, U.H., Jackson, M., Moore, P.L., Lappegard, G., and Kohler, J., 2003, Effects of basal debris on glacier flow: Science, v. 301, p. 81–84.

Iverson, N.R., Helanow, C., and Zoet, L.K., 2020, Debris-bed friction during glacier sliding with ice–bed separation: Annals of Glaciology, p. 1–7, doi:10.1017/aog.2019.46.

Jaeger, J.C., Cook, N.G., and Zimmerman, R. W., 2007, Fundamentals of Rock Mechanics: Malden, MA, Blackwell Publishing.

Kamb, B., 1987, Glacier surge mechanism based on linked cavity configuration of the basal water conduit system: Journal of Geophysical Research: Solid Earth, v. 92, p. 9083–9100.

Kamb, B., 1970, Sliding motion of glaciers: theory and observation: Reviews of Geophysics, v. 8, p. 673–728.

Koellner, S., Parizek, B.R., Alley, R.B., Muto, A., and Holschuh, N., 2019, The impact of spatially-variable basal properties on outlet glacier flow: Earth and Planetary Science Letters, v. 515, p. 200–208.

Lambe, T.W., and Whitman, R.V., 1979, Soil Mechanics, SI Version: New York, John Wiley & Sons.

Lliboutry, L., 1968, General theory of subglacial cavitation and sliding of temperate glaciers: Journal of Glaciology, v. 7, p. 21–58.

Lusardi, B.A., and Dengler, E.L., 2017, Minnesota at a glance quaternary glacial geology:

MacGregor, K.R., Anderson, R.S., and Waddington, E.D., 2009, Numerical modeling of glacial erosion and headwall processes in alpine valleys: Geomorphology, v. 103, p. 189–204.

McCarthy, C., Savage, H., and Nettles, M., 2017, Temperature dependence of ice-on-rock friction at realistic glacier conditions: Philosophical Transactions of the Royal Society A: Mathematical, Physical and Engineering Sciences, v. 375, p. 20150348, doi:10.1098/rsta.2015.0348.

Muto, A., Anandakrishnan, S., Alley, R.B., Horgan, H.J., Parizek, B.R., Koellner, S., Christianson, K., and Holschuh, N., 2019, Relating bed character and subglacial morphology using seismic data from Thwaites Glacier, West Antarctica: Earth and Planetary Science Letters, v. 507, p. 199–206.

Nick, F.M., Vieli, A., Andersen, M.L., Joughin, I., Payne, A., Edwards, T.L., Pattyn, F., and van de Wal, R.S., 2013, Future sea-level rise from Greenland's main outlet glaciers in a warming climate: Nature, v. 497, p. 235–238.

Nye, J.F., 1969, A calculation on the sliding of ice over a wavy surface using a Newtonian viscous approximation: Proceedings of the Royal Society of London. A. Mathematical and Physical Sciences, v. 311, p. 445–467.

Nye, J.F., 1970, Glacier sliding without cavitation in a linear viscous approximation: Proceedings of the Royal Society of London. A. Mathematical and Physical Sciences, v. 315, p. 381–403.

Powers, M.C., 1953, A new roundness scale for sedimentary particles: Journal of Sedimentary Research, v. 23, p. 117–119.

Rempel, A.W., and Meyer, C.R., 2019, Premelting increases the rate of regelation by an order of magnitude: Journal of Glaciology, v. 65, p. 518–521.

Schweizer, J., and Iken, A., 1992, The role of bed separation and friction in sliding over an undeformable bed: Journal of Glaciology, v. 38, p. 77–92.

Shoemaker, E.M., 1986, Debris-influenced sliding laws and basal debris balance: Journal of Glaciology, v. 32, p. 224–231.

Thøgersen, K., Gilbert, A., Schuler, T.V., and Malthe-Sørenssen, A., 2019, Rate-and-state friction explains glacier surge propagation: Nature communications, v. 10, p. 1–8.

Vivian, R., 1980, The nature of the ice-rock interface: the results of investigation on 20,000 m^2 of the rock bed of temperate glaciers: Journal of Glaciology, v. 25, p. 267–277.

Vivian, R., and Bocquet, G., 1973, Subglacial cavitation phenomena under the glacier d'Argentière, Mont Blanc, France: Journal of Glaciology, v. 12, p. 439–451.

Watts, P.A., 1974, Inclusions in ice [PhD thesis]: University of Bristol.

Weertman, J., 1957, On the sliding of glaciers: Journal of Glaciology, v. 3, p. 33–38.

Wettlaufer, J.S., and Worster, M.G., 1995, Dynamics of premelted films: Frost heave in a capillary: Physical Review E, v. 51, p. 4679–4689, doi:10.1103/PhysRevE.51.4679.

Willis, J.K., and Church, J.A., 2012, Regional sea-level projection: Science, v. 336, p. 550–551.

Zoet, L.K., Carpenter, B., Scuderi, M., Alley, R.B., Anandakrishnan, S., Marone, C., and Jackson, M., 2013, The effects of entrained debris on the basal sliding stability of a glacier: Journal of Geophysical Research: Earth Surface, v. 118, p. 656–666, doi:10.1002/jgrf.20052.

APPENDIX. FULL TIME SERIES

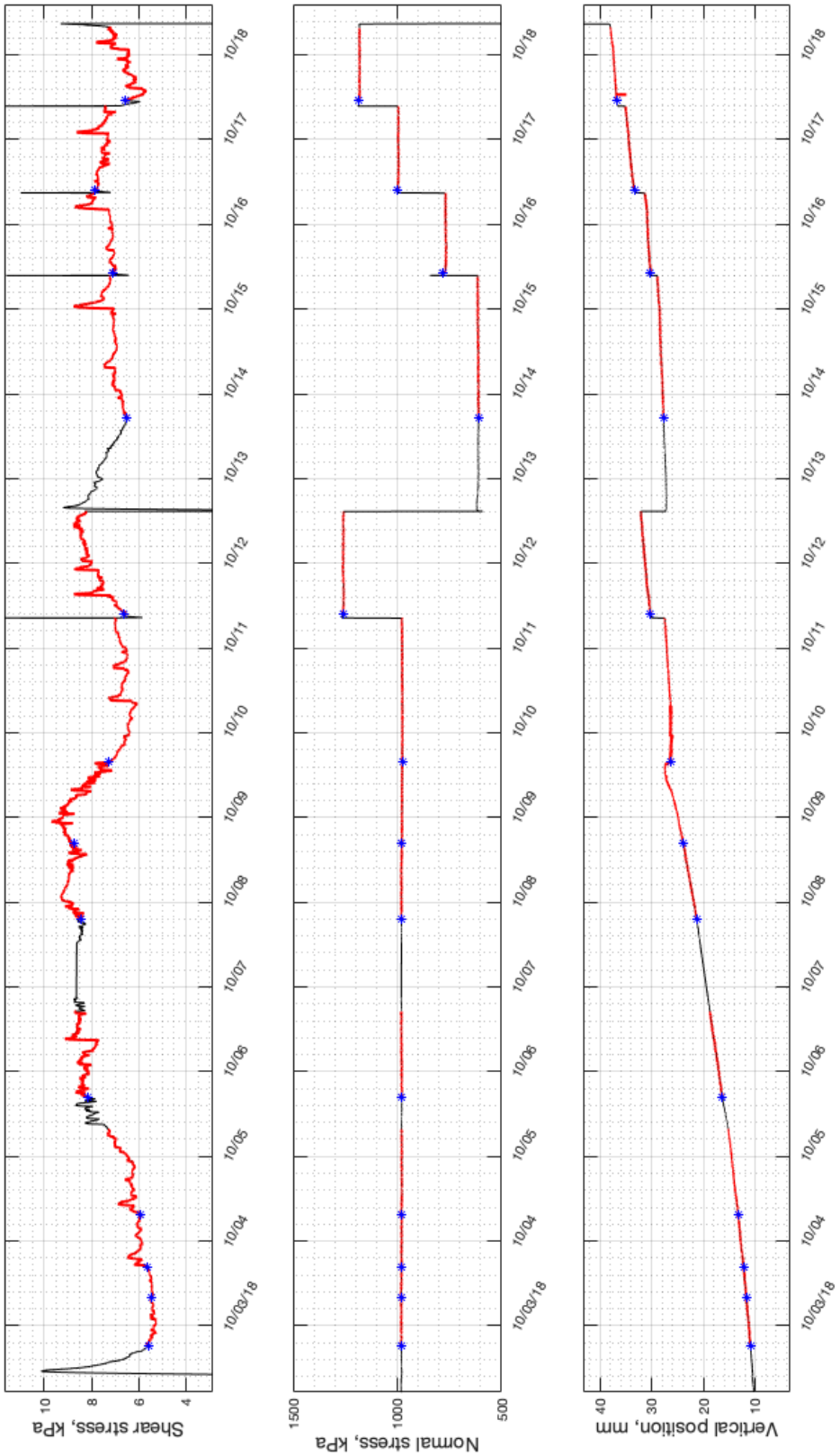

Figure A1. Experiment 1 time series. Red highlights the time over which measurements are made. Blue stars mark the beginning of measurement periods.

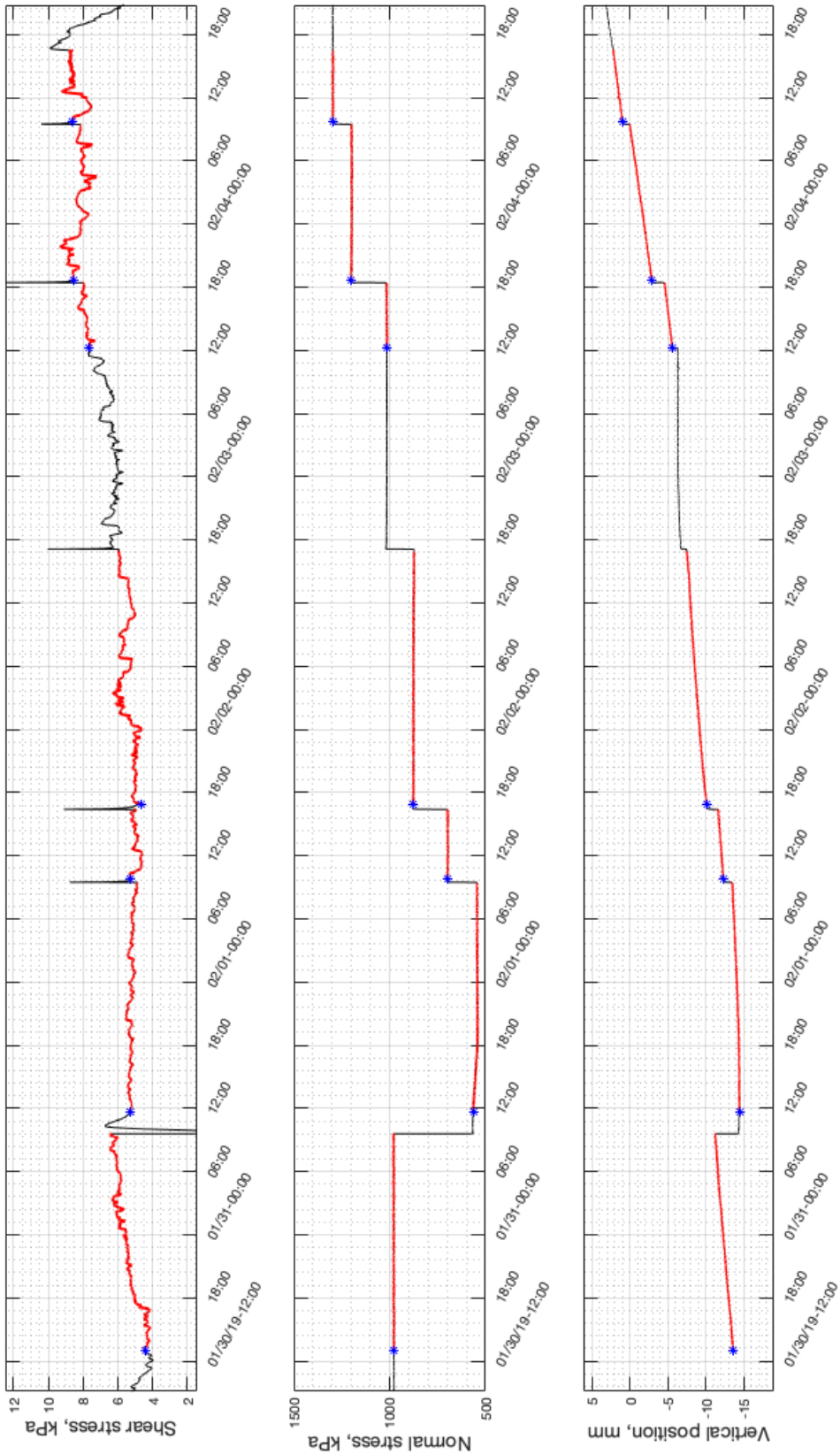

Figure A2. Experiment 2 time series.

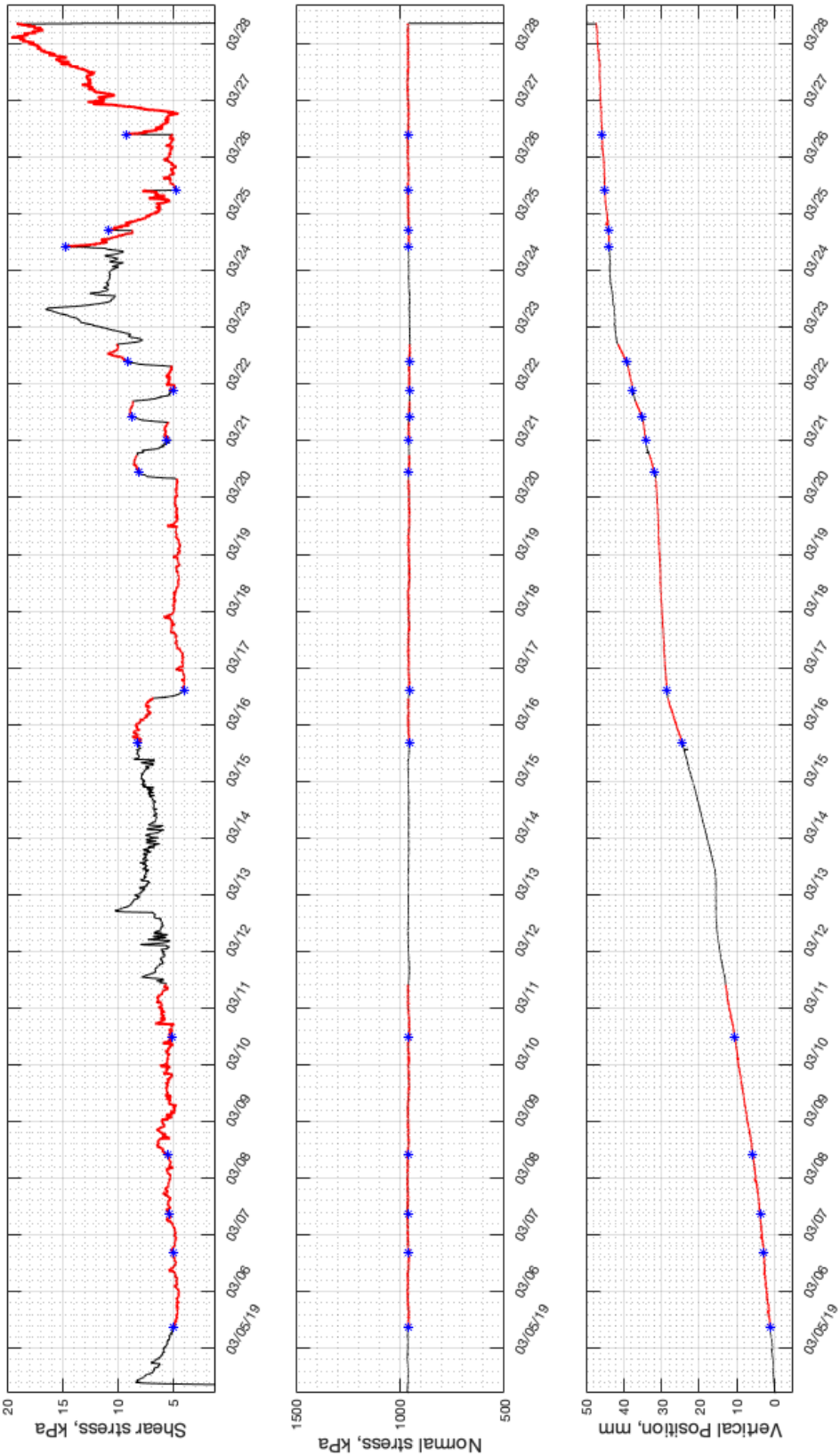

Figure A3. Experiment 3 time series.

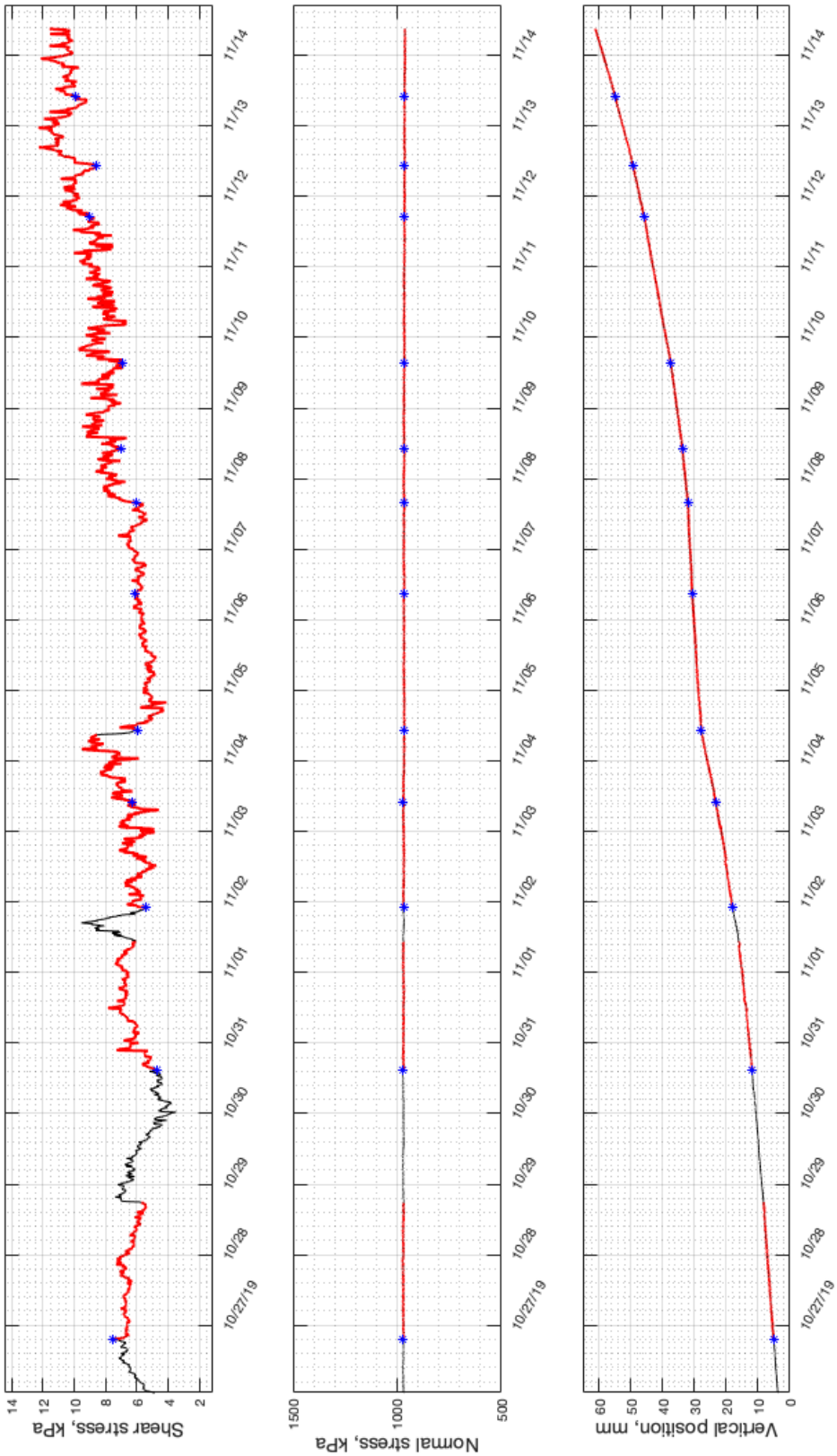

Figure A4. Experiment 4 time series.